

Microstructure Characterization and Mechanical Properties of Polymer-Derived $(\text{Hf}_x\text{Ta}_{1-x})\text{C}/\text{SiC}$ Ceramic Prepared upon Field-Assisted Sintering Technique/Spark Plasma Sintering

Nathalie Thor,* Georg Winkens, Jan Bernauer, Nils-Christian Petry, Katharina Beck, Jin Wang, Ruth Schwaiger, Ralf Riedel, Ute Kolb, Maren Lepple, and Astrid Pundt

The high-temperature microstructural evolution and mechanical properties of two SiC-based polymer-derived ceramics with different Hf:Ta molar ratios are investigated using electron microscopy techniques and manipulated by nanoindentation. The as-pyrolyzed ceramic powder consists of an amorphous $\text{Si}(\text{Hf}_x\text{Ta}_{1-x})\text{C}(\text{N},\text{O})$ structure (where $x=0.2, 0.7$) with localized nanocrystalline transition metal carbides (TMCs). Subsequent application of the field-assisted sintering technique (FAST) for high-temperature consolidation results in a crystalline $(\text{Hf}_x\text{Ta}_{1-x})\text{C}/\text{SiC}$ ultra-high temperature ceramic nanocomposite. The microstructure contains powder particle-sized grains and sinter necks between the former powder particles. The powder particles consist of a β -SiC matrix and small TMCs. Large TMCs are observed on the internal surfaces of former powder particles. This is due to the pulsed direct current and the resulting Joule heating that facilitates diffusion as well as oxygen impurities. Sinter necks of large β -SiC grains form during the FAST process. The microstructural regions are assessed using high-throughput nanoindentation. The hardness for $\text{SiC}/(\text{Hf}_{0.7}\text{Ta}_{0.3})\text{C}$ is measured on the formed grains and the sinter necks giving mean hardness values of about 27 and 37 GPa, respectively.

1. Introduction


Transition metal carbides (TMCs), like HfC and TaC, are defined as ultra-high temperature ceramics (UHTCs) possessing melting points above 3000 °C.^[1–4] In particular, the solid solution of $(\text{Hf}_{0.2}\text{Ta}_{0.8})\text{C}$ (Ta_4HfC_5) is a well-known compound possessing the highest ever known melting temperature of a solid material ($T_m = 4215 \text{ K} = 3985 \text{ °C}$).^[5]

UHTCs display a number of beneficial properties including high refractoriness, chemical stability, excellent electrical and thermal conductivity, high-temperature strength, high toughness, creep resistance, high hardness values, and high elastic moduli.^[3,4,6–13] This unique combination of properties makes them promising materials for a wide range of high-temperature structural applications.^[1,12,14,15]

N. Thor, U. Kolb
Institute of Applied Geoscience
Technical University Darmstadt
Schnittspahnstraße 9, D-64287 Darmstadt, Germany
E-mail: nathalie.thor@tu-darmstadt.de

G. Winkens, A. Pundt
Institute for Applied Materials (IAM)
Karlsruhe Institut für Technologie (KIT)
Engelbert-Arnold-Straße 4, D-76131 Karlsruhe, Germany

J. Bernauer, R. Riedel
Institute of Materials Science
Technical University Darmstadt
Otto-Berndt-Straße 3, D-64287 Darmstadt, Germany

 The ORCID identification number(s) for the author(s) of this article can be found under <https://doi.org/10.1002/adem.202301841>.

© 2024 The Authors. Advanced Engineering Materials published by Wiley-VCH GmbH. This is an open access article under the terms of the Creative Commons Attribution-NonCommercial License, which permits use, distribution and reproduction in any medium, provided the original work is properly cited and is not used for commercial purposes.

DOI: 10.1002/adem.202301841

N.-C. Petry, K. Beck
Materials and Corrosion
DECHEMA Research Institute
Theodor-Heuss-Allee 25, D-60486 Frankfurt am Main, Germany

J. Wang, R. Schwaiger
Institute of Energy and Climate Research (IEK)
Forschungszentrum Jülich GmbH
Wilhelm-Johnen Straße, D-52428 Jülich, Germany

R. Schwaiger
Chair of Energy Engineering Materials
RWTH Aachen University
D-52056 Aachen, Germany

U. Kolb
Centre for High Resolution Electron Microscopy (EMC-M)
Johannes Gutenberg University Mainz
Duesbergweg 10-14, 55128 Mainz, Germany

M. Lepple
Department of Inorganic and Analytical Chemistry
Justus-Liebig-University Giessen
Heinrich-Buff-Ring 17, D-35392 Giessen, Germany

However, pure UHTCs are limited in their widespread application due to their poor sinterability, caused by their strong covalent bonds and low intrinsic self-diffusion coefficient.^[3,7,10,16–19] A successful way to overcome these sintering issues is adjusting the sintering parameter, i.e., the use of high sintering temperatures in the range of 2000 °C,^[17] high heating rates (up to 1000 °C min⁻¹), moderate pressures in the range of 40 up to 100 MPa, and the addition of suitable sintering aids such as silica-formers like SiC,^[10,20,21] Si₃N₄^[22] or silicides (MoSi₂, TaSi₂).^[3,23,24] In particular, the utilization of silica formers brings another decisive advantage. It increases the oxidation resistance due to the formation of a passivating silica layer, which is protective at least up to ≈1700 °C.^[25–27] This is indeed helpful as TMCs show a relatively poor oxidation resistance.^[4,18,26,28]

The most common way to synthesize ceramics is the powder metallurgy (PM) route and subsequent densification via conventional sintering (e.g., hot pressing, high-pressure sintering, and pressureless sintering).^[19] However, these methods hinder the processing of complex-shaped ceramics.^[29,30] The polymer-derived ceramic (PDC) route is an advanced chemical approach to synthesize multielement silicon-based ceramics.^[29,31,32] It provides a facile and inexpensive preparation of unique ceramic compositions with tailored phase compositions, microstructures, and property profiles.^[33] Commercially available, polymeric precursors such as polycarbosilane, polysilazane, or polysiloxane in combination with metal-modified complexes are used to prepare ultra-high temperature ceramic nanocomposites (UHTC-NCs) via thermal pyrolysis.^[33,34] High-temperature environments cause the UHTCs such as HfN, HfC, TiC, TaC, or ZrC to precipitate in situ as secondary phases into a Si-based matrix phase (e.g., SiC or Si₃N₄).^[29] During the last two decades, the incorporation of transition metal complexes became popular and several ceramic composites were prepared via the PDC route: SiHfN,^[35] SiHfCN,^[36] SiHf(B)CN,^[37,38] SiHfCNO,^[39] HfO₂/SiCN(O),^[40] SiHfBOC,^[41] SiOC/ZrO₂,^[42] ZrC-SiC,^[43,44] SiZr(B)CN,^[31] SiTiN,^[45] and SiHfTa(C)N.^[46] In 2018, Wen et al.^[5] first reported on the synthesis of a dense polymer-derived monolithic Hf_xTa_{1-x}C/SiC nanocomposite containing well-controlled Hf:Ta ratios, consolidated via the field-assisted sintering technique (FAST).^[47]

FAST, also known as spark plasma sintering (SPS), is an emerging method that allows various powders to be sintered rapidly into nearly fully dense bodies with fine-grained micro- and nanostructures.^[17,19,47–51] During FAST, unlike hot pressing (HP), a pulsed electric current (1000–8000 A) is passed through a conducting pressure die and also through the containing powder sample (when the powders are electrically conductive),^[7,17,48,51] while an additional high uniaxial pressure (up to 100 MPa), high temperatures (up to 2400 °C), and high heating rates (up to 1000 K min⁻¹) are applied.^[7,47,48,52] While processing under HP takes several hours, FAST only takes a few minutes for densification.^[7,47,48]

Recent literature focuses on the synthesis of nearly fully dense Hf/Ta containing UHTC-NCs^[3,5,10] and on the improved short-term oxidation resistance.^[53,54] Especially, ceramic composites with a molar Hf:Ta ratio of 7:3 show an improved oxidation resistance due to the formation of the Hf₆Ta₂O₁₇ superstructure, showing no phase transformations up to temperatures of ≈2200 °C and therefore making it a potential candidate

for high-temperature applications.^[55–58] To the best of our knowledge, there is no published data dealing with a detailed analysis of the microstructural evolution of polymer-derived Si-Hf-Ta-C ceramic powders consolidated into dense Hf_xTa_{1-x}C/SiC ceramics via FAST/SPS.

To date, it has not fully been understood how the sintering mechanisms and densification kinetics influence the emerging microstructure.^[59,60] To permit control of the microstructural evolution at high- and ultra-high-temperature applications, a general understanding of the correlation of the obtained microstructures to the initial ceramic powders and the processing parameters is mandatory.^[61]

In a recent study, we reported on the microstructural evolution of a novel Si(Hf_xTa_{1-x})C(N) polymer-derived powder sample upon high-temperature annealing. We proposed a microstructural evolution model on the development of bulk and surface regions in individual powder particles. Grain coarsening of TMCs in surface-near regions and the influence of thermal decomposition reactions in combination with diffusion phenomena in Si(Hf,Ta)C(N)-based PDCs were studied.^[46]

In this investigation, our primary focus is on examining the microstructural evolution of two Si(Hf_xTa_{1-x})C(N,O) (with $x = 0.2, 0.7$) polymer-derived ceramic powders and their consolidation into dense (Hf_xTa_{1-x})C/SiC nanocomposites via FAST. We present a comprehensive study of the macro- and microstructural evolution, starting from the as-pyrolyzed powders into the consolidated (Hf_xTa_{1-x})C/SiC PDCs. Moreover, we employed high-throughput nanoindentation and statistical analysis to accurately determine the hardness and Young's modulus of the constituent microstructural regions within the bulk samples. The obtained results offer valuable insights into the underlying mechanisms governing the microstructural evolution of these advanced ceramic materials, providing critical information for the design and development of high-performance materials for demanding applications.

2. Results

In general, the Ta-rich (Hf_{0.2}Ta_{0.8})C/SiC and Hf-rich (Hf_{0.7}Ta_{0.3})C/SiC PDCs show very similar microstructural characteristics as well as comparable mechanical properties. This is shown exemplarily in **Figure 1** for the two different composites after the FAST process. Therefore, microstructural results and mechanical properties in this study are discussed only for the Hf-rich (Hf_{0.7}Ta_{0.3})C/SiC sample.

2.1. Chemical Composition and Phase Assemblage

The chemical composition of the metal-containing ceramic after pyrolysis and after sintering is listed in **Table 1**. Both ceramics contain the elements Si, Hf, Ta, C, N, and O and differ mainly in the N and O concentrations (cf. Table 1). XRD patterns of the ceramic powder and the sintered bulk ceramic are presented in **Figure 2**. The ceramic powder pyrolyzed at 1000 °C in Argon is X-ray amorphous, showing no sharp diffraction peak. However, a very broad peak at $2\theta = 36^\circ$ corresponding to the (111) peak of β -SiC is detected, as shown in **Figure 2**. The XRD pattern of the sintered dense bulk ceramic indicates a

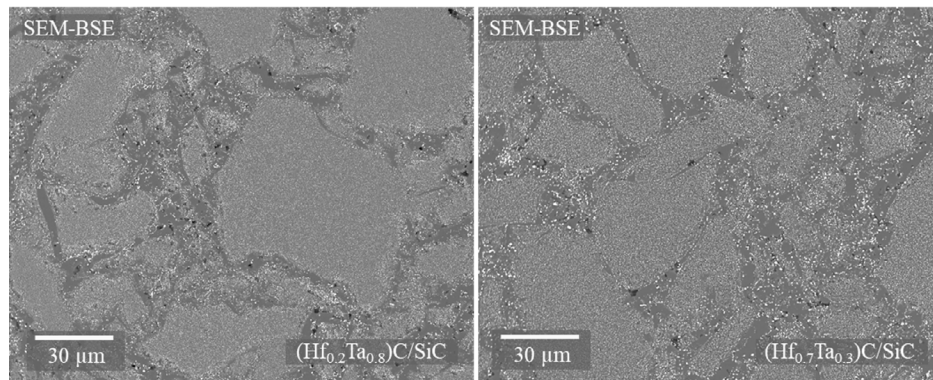


Figure 1. A comparison of the microstructure of the Ta-rich $(\text{Hf}_{0.2}\text{Ta}_{0.8})\text{C}/\text{SiC}$ (left) and Hf-rich $(\text{Hf}_{0.7}\text{Ta}_{0.3})\text{C}/\text{SiC}$ UHTC-NC after consolidation is shown.

Table 1. Chemical composition of the as-pyrolyzed $\text{Si}(\text{Hf}_{0.7}\text{Ta}_{0.3})\text{C}(\text{N},\text{O})$ and sintered $(\text{Hf}_{0.7}\text{Ta}_{0.3})\text{C}/\text{SiC}$ ceramics in wt% and at% and the respective empirical formulas.

| Sample | Elemental analysis | | | | | | |
|--|--------------------|---|------|------|-------|------|------|
| | | Si | Hf | Ta | C | N | O |
| $\text{Si}(\text{Hf}_{0.7}\text{Ta}_{0.3})\text{C}(\text{N},\text{O})$ | [wt%] | 46.9 | 11.1 | 3.75 | 29.03 | 3.64 | 4.01 |
| $\text{Si}(\text{Hf}_{0.7}\text{Ta}_{0.3})\text{C}(\text{N},\text{O})$ | [at%] | 35.68 | 1.33 | 0.44 | 51.64 | 5.55 | 5.36 |
| Empirical formula | | $\text{Si}(\text{Hf}_{0.037}\text{Ta}_{0.012})\text{C}_{1.447}\text{N}_{0.156}\text{O}_{0.150}$ | | | | | |
| | Elemental analysis | | | | | | |
| | | Si | Hf | Ta | C | N | O |
| $(\text{Hf}_{0.7}\text{Ta}_{0.3})\text{C}/\text{SiC}$ | [wt%] | 51.8 | 12.4 | 4.25 | 29.34 | 0.31 | 0.17 |
| $(\text{Hf}_{0.7}\text{Ta}_{0.3})\text{C}/\text{SiC}$ | [at%] | 41.79 | 1.57 | 0.53 | 55.46 | 0.50 | 0.24 |
| Empirical formula | | $\text{Si}(\text{Hf}_{0.038}\text{Ta}_{0.013})\text{C}_{1.325}\text{N}_{0.012}\text{O}_{0.006}$ | | | | | |

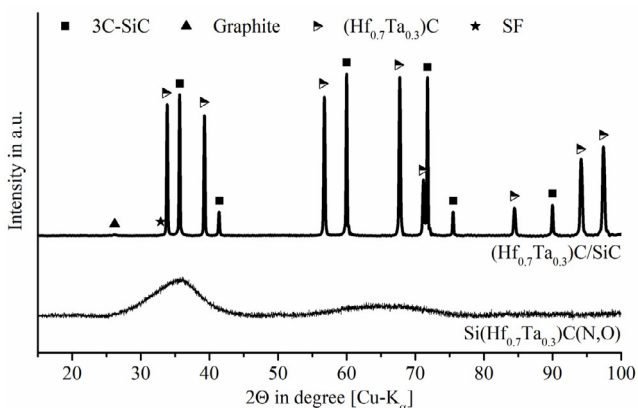


Figure 2. XRD pattern of the as-pyrolyzed $\text{Si}(\text{Hf}_{0.7}\text{Ta}_{0.3})\text{C}(\text{N},\text{O})$ sample (bottom) and the sintered $(\text{Hf}_{0.7}\text{Ta}_{0.3})\text{C}/\text{SiC}$ (top).

crystalline ceramic with three phases present: β -SiC (3C-SiC), the TMC $(\text{Hf}_x\text{Ta}_{1-x})\text{C}$, and graphitic carbon. The pronounced six sharp peaks at $2\theta = 35.7^\circ$, 41.5° , 60.1° , 71.9° , 75.6° , and 90.2° are attributed to the diffractions of (111), (200), (220), (311), (222), and (400) planes of β -SiC (PDF 29–1129) indexed with a closed rectangle symbol. The indication of the diffraction peak

around $2\theta = 33.7^\circ$, depicted with the star symbol is ascribed to stacking faults (SF) in SiC, whereas the sharp peak of the TMC is superimposing the weak SF peak. This phenomenon is discussed later in Section 2.3.4 (TEM). The remaining sharp peaks are indexed as TMC $(\text{Hf}_{0.7}\text{Ta}_{0.3})\text{C}$, depicted with a half-filled, lying triangle symbol (PDF 19-6861). The small peak at $2\theta = 26.2^\circ$ is attributed to graphitic carbon, indexed with a closed triangle.

2.2. Microstructure of As-Pyrolyzed $\text{Si}(\text{Hf}_{0.7}\text{Ta}_{0.3})\text{C}(\text{N},\text{O})$ Powders

Detailed electron microscopic investigations on as-pyrolyzed $\text{Si}(\text{Hf}_{0.7}\text{Ta}_{0.3})\text{C}(\text{N},\text{O})$ powder particles were carried out via SEM and TEM in conjunction with EDS and SAED. **Figure 3** shows a typical SEM-BSE micrograph, giving a general overview of the starting (as-pyrolyzed) PDC powder sample. The powder reveals a featureless microstructure, no individual grains were observed via SEM imaging (cf. Figure 3a). The EDS spectrum in Figure 3b was taken from a representative point measurement at the surface of the powder particle. Figure 3b shows the presence of Si ($K_\alpha = 1.74$ keV), Hf ($M_\alpha = 1.646$ keV, $L_\alpha = 7.899$ keV), Ta ($M_\alpha = 1.712$ keV, $L_\alpha = 8.146$ keV), C ($K_\alpha = 0.277$ keV), N ($K_\alpha = 0.392$ keV), and a relatively strong O peak ($K_\alpha = 0.525$ keV). The composition obtained via EDS is in good agreement with the elemental analyses shown in Table 1.

TEM analyses allow a more detailed understanding of the microstructure compared to SEM. TEM-BF, HR-TEM images, SAED patterns, fast Fourier transform (FFT) images, and EDS analysis of the as-pyrolyzed powders are depicted in **Figure 4**. In agreement with the X-ray amorphous XRD pattern (cf. Figure 2) and SEM analysis (cf. Figure 3), these powder particles exhibit a mostly featureless appearance. The amorphous structure is evident due to the homogeneous amplitude contrast in the TEM image in Figure 4a and the diffuse halo ring pattern as shown in the SAED pattern in Figure 4c. The chemical analysis of the amorphous glass network via EDS in TEM is shown exemplarily in Figure 4d. The spectrum depicts the presence of Si, Hf, Ta, C, N, and O. These results are therefore in good agreement with the SEM results and those of the elemental analyses shown in Table 1. Small amounts of N are detected

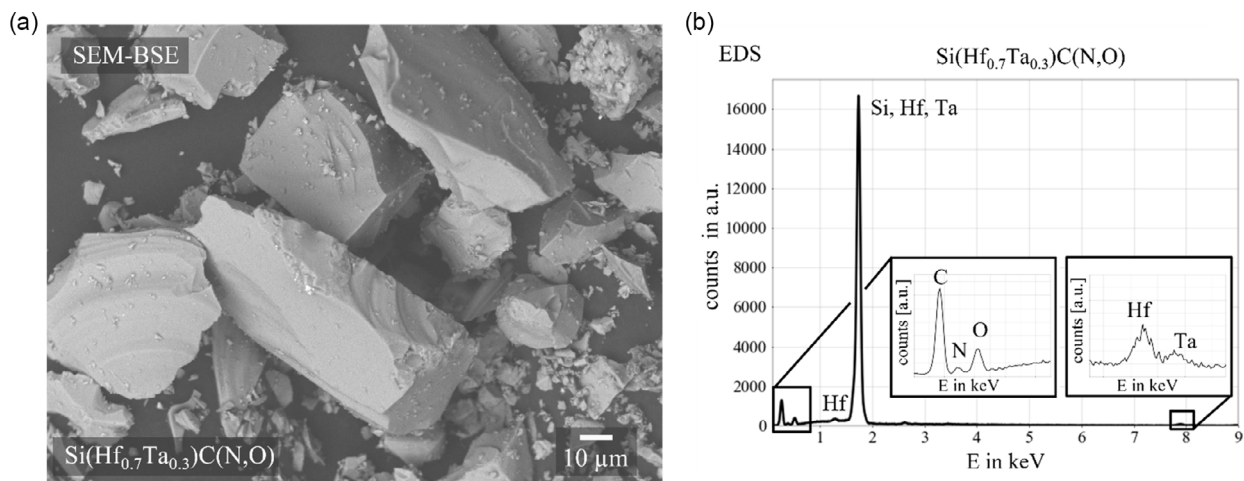


Figure 3. a) SEM-BSE micrograph of the as-pyrolyzed $\text{Si}(\text{Hf}_{0.7}\text{Ta}_{0.3})\text{C}(\text{N},\text{O})$ ceramic showing the featureless surface morphology; b) EDS spectrum from the surface of the amorphous PDC containing the elements Si (K_{α}), Hf (M_{α} , L_{α}), Ta (M_{α} , L_{α}), C (K_{α}), N (K_{α}), and O (K_{α}).

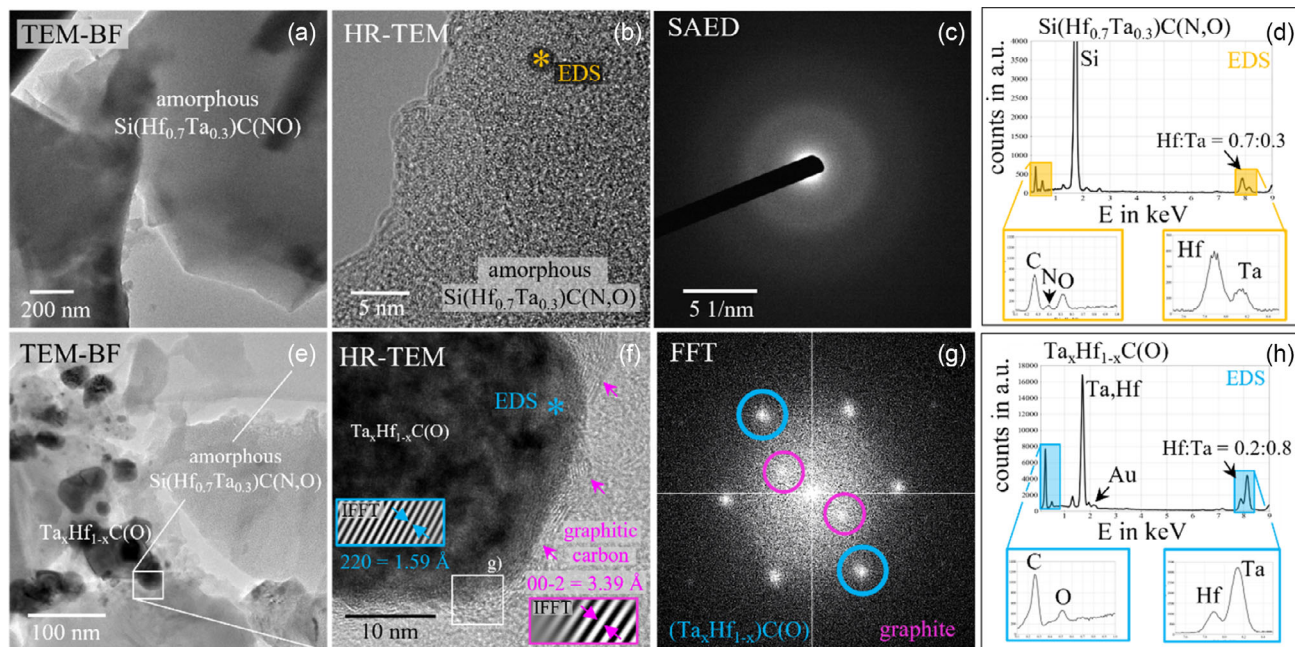


Figure 4. a,e) TEM-BF images; b,f) HR-TEM micrographs; c) SAED pattern; d) EDS spectrum showing a mostly amorphous $\text{Si}(\text{Hf}_{0.7}\text{Ta}_{0.3})\text{C}(\text{N},\text{O})$ powder pyrolyzed at 1000 °C in Ar (indicated in b) with the star symbol; g) FFT image; and h) EDS spectrum showing the chemistry of the $(\text{Ta}_x\text{Hf}_{1-x})\text{C}(\text{O})$ nanocrystal (indicated with the blue star symbol in f).

and reasonable due to the nitrogen occurrence within the structure of PDMAT and TDEAH. The incorporation of oxygen into the glass network of the predominantly amorphous ceramic is due to polymer processing, as some minor amounts of oxygen are difficult to avoid.

In the amorphous $\text{Si}(\text{Hf}_{0.7}\text{Ta}_{0.3})\text{C}(\text{N},\text{O})$ glass network, a mean Hf:Ta ratio of 0.7:0.3 was analyzed using EDS point measurements (cf. Figure 4d), fitting very well to the anticipated Hf:Ta ratio. While the XRD pattern of the as-pyrolyzed sample in Figure 2 indicated an X-ray amorphous structure, TEM

investigations reveal a small number of Hf, Ta-rich nanoparticles. The distinct observation of nanoparticles was confirmed via HR-TEM, indicating that the microstructure of the as-pyrolyzed powder ceramic is defined as pseudo-amorphous instead of fully amorphous. Figure 4e depicts two distinct contrasts, showing the primarily amorphous $\text{Si}(\text{Hf}_{0.7}\text{Ta}_{0.3})\text{C}(\text{N},\text{O})$ structure and some darker appearing Hf, Ta-rich nanoparticles. The particle size of the nanoparticles ranges from ≈ 5 nm up to 100 nm (Figure 4e,f). EDS analysis in combination with HR-TEM imaging, electron diffraction, and FFT images in

Figure 4f–h reveal an intermetallic compound phase with small amounts of oxygen incorporated, namely, $(\text{Ta}_x\text{Hf}_{1-x})\text{C}(\text{O})$, known as TMC. The mean value of the Hf:Ta ratio on the nanoparticles is $0.23:0.77 \pm 0.04$ and was determined by measuring 18 individual EDS point measurements on individual nanoparticles. The uncertainty is based on a standard uncertainty multiplied by a coverage factor $k = 2$. This ratio no longer corresponds to the Hf:Ta ratio of the residual amorphous $\text{Si}(\text{Hf}_{0.7}\text{Ta}_{0.3})\text{C}(\text{N},\text{O})$ microstructure with a Hf:Ta ratio of 0.7:0.3 (compare the heights of the Hf:Ta peaks in Figure 4d with Figure 4h). TMC nanoparticles are encapsulated with a thin 2–4 nm graphitic carbon layer/shell, as can be seen in the HR-TEM in Figure 4f (see inset indicated by white square) and the corresponding FFT image in Figure 4g. These carbon shells have already been reported in literature.^[5]

2.3. Microstructure of Consolidated $(\text{Hf}_{0.7}\text{Ta}_{0.3})\text{C}/\text{SiC}$

2.3.1. Optical Light and SEM

The monolithic $(\text{Hf}_{0.7}\text{Ta}_{0.3})\text{C}/\text{SiC}$ bulk ceramic was studied *ex situ* by OLM and SEM to assess the microstructure after sintering. Correlative light and electron microscopy (CLEM) enables us to show and compare the exact same area of interest with two different microscopy methods in Figure 5. The optical light micrographs and correlated SEM-BSE images of the sintered $(\text{Hf}_{0.7}\text{Ta}_{0.3})\text{C}/\text{SiC}$ composites are shown. In general, OLM and SEM images show three different microstructural regions, which constitute 1) the former powder particles, 2) the sinter necks, and 3) the residual porosity within the ceramics.

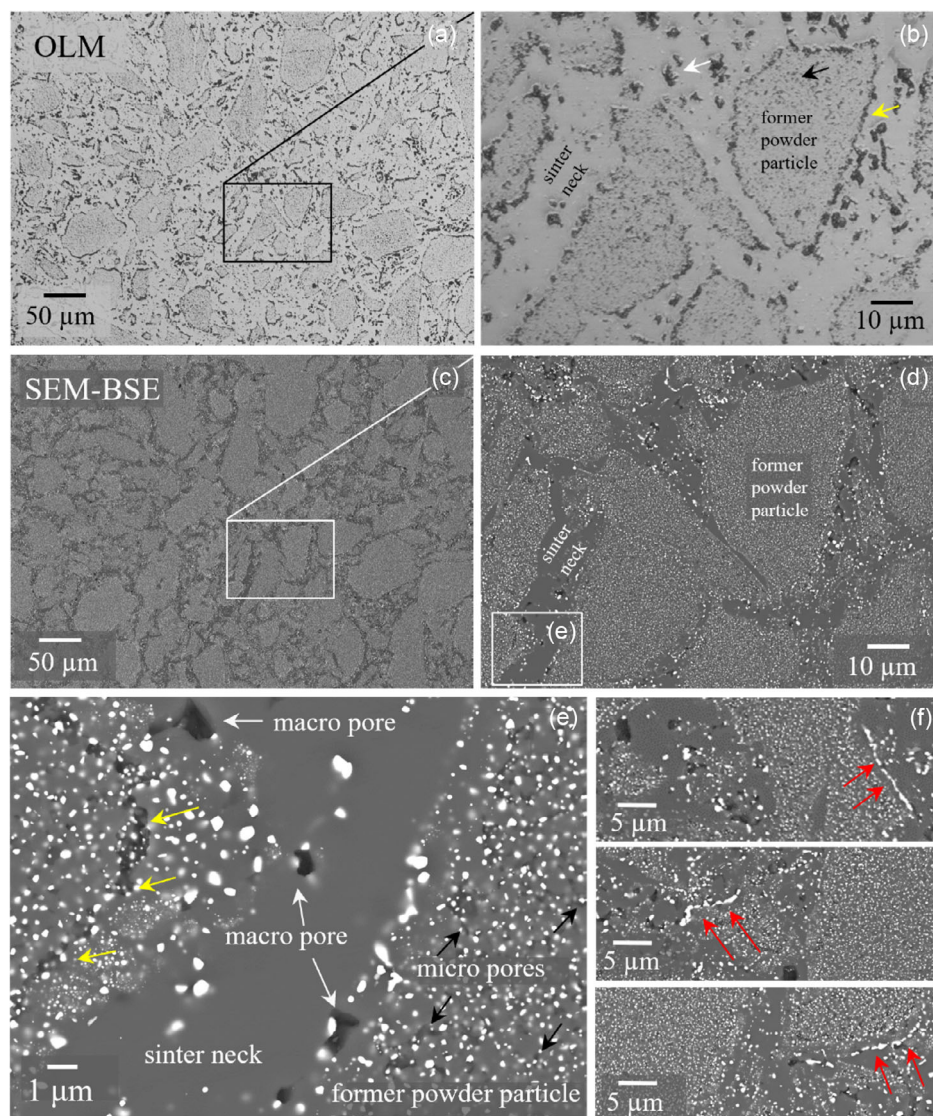


Figure 5. a,b) CLEM showing three distinct microstructure regions of the sintered monolithic $(\text{Hf}_{0.7}\text{Ta}_{0.3})\text{C}/\text{SiC}$ ceramic: former powder particles, sinter necks, and pores can be observed via OLM images and c,d) SEM-BSE images. The three arrows (white, black, and yellow) shown in b,e) indicate the different porosities, occurring in the sinter neck (white arrow), in the former powder particle (black arrow), and in the contact zone between the sinter neck and the former powder particle (yellow). The white rectangle in (d) is shown as a magnified SEM image in (e), presenting a sinter neck in the middle and two former powder particles on the left and right, respectively. In the SEM image in f) TMCs appear very close together.

The former powder particles and sinter necks are labeled as such in Figure 5b,d. These two microstructural components make up the majority of the microstructure. However, the porosity is also part of the microstructure, it appears in three different forms, depicted with three different colored arrows in Figure 5b (white, black, and yellow). Porosity within the former powder particles is depicted with the black arrow in Figure 5b,e. The images show very small-scaled intragranular pores reaching pore sizes of ≈ 30 nm. The distribution of small-scaled pores in the former powder particles results in an overall darker appearance in the OLM image in Figure 5a,b due to diffuse scattering of the light. Therefore, in OLM, regions of the former powder particle appear darker compared to the sinter necks.

Further, porosity can be observed at the interface between the former powder particles and the sinter necks (cf. yellow arrows in Figure 5b,e). In addition, the OLM and SEM-BSE images in Figure 5b,e show large macropores (white arrows) with a significant variation in pore morphology and different pore sizes (up to $3 \mu\text{m}$), particularly in the area of the sinter necks.

In SEM-BSE micrographs (Figure 5c–f), the regions of the former powder particles constitute two finely dispersed phases. Due to XRD diffraction, chemical analysis (EDS) in combination with electron diffraction (SAED in TEM, cf. Section 2.3.4), the dark-appearing phase in SEM-BSE micrographs is characterized as silicon carbide (SiC). The bright-appearing particles are defined as solid solutions of TMCs, here specifically $(\text{Hf}_{0.7}\text{Ta}_{0.3})\text{C}$. Therefore, the microstructure within the former powder particles is ascribed as nanosized, homogeneously distributed TMCs embedded in a SiC matrix. With this, the microstructure of the former powder particles differs fundamentally from the microstructure in the sinter necks. Sinter necks mainly

constitute SiC with enlarged grain sizes of TMCs. TMCs within the sinter necks often occur near the internal surfaces of the former powder particles.

Another interesting microstructural feature was observed near the internal surfaces of the former powder particles and is depicted in Figure 5f. There are TMCs that are increased in grain size and appear lined up in the microstructure (indicated with red arrows).

2.3.2. Porosity Determined via Quantitative Image Analysis and Archimedes Drainage

The residual porosity found in the $(\text{Hf}_{0.7}\text{Ta}_{0.3})\text{C}/\text{SiC}$ sample is observable via SEM imaging on polished cross-sections of the sintered bulk sample. As determined with image analysis, the detected cross-sectional area of pores related to the total area gives an area density of 4.6%. The relatively high material density of up to $\approx 95\%$ in the ceramic bulk sample can be attributed to the consolidation via FAST. In total, eleven individual images from different regions of the sample were taken and evaluated for the selected magnification of $1000\times$. **Figure 6** shows exemplarily one BSE image in a), the quantitatively analyzed pores depicted in blue color in b), and the final image, which concludes after thresholding in c). The overall results from eleven images give a mean porosity value with the uncertainty of 4.6 ± 0.9 area% for the $(\text{Hf}_{0.7}\text{Ta}_{0.3})\text{C}/\text{SiC}$. The reported uncertainty is based on a standard uncertainty multiplied by a coverage factor $k = 2$, providing a level of confidence of approx. 95%.^[62] Figure 6d depicts a $10000\times$ magnified region of the former powder particle. It shows the presence of micropores, which are depicted in blue. Further, theoretical cross-sections of nanoindentation imprints are drawn

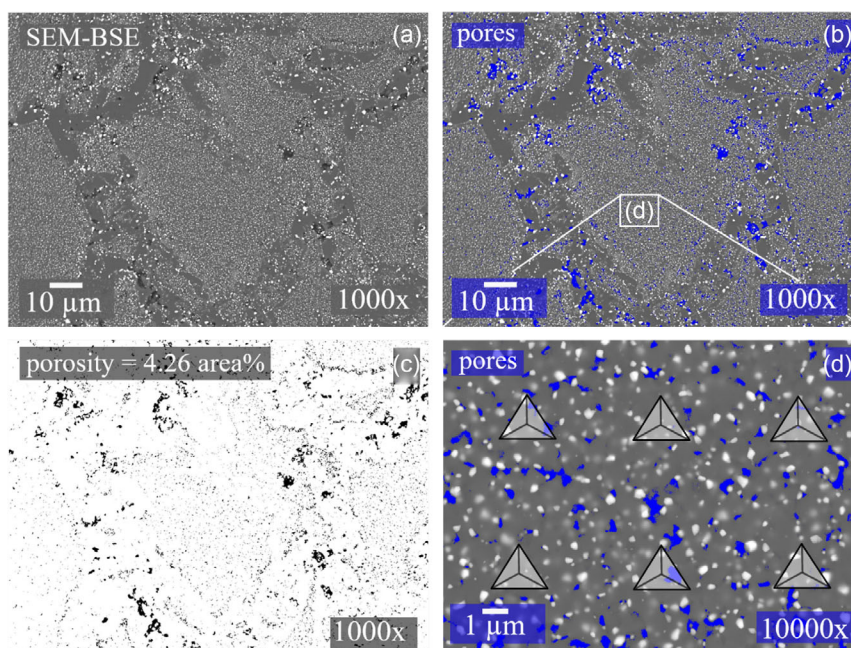


Figure 6. SEM-BSE image used to determine the value of the closed porosity in the $(\text{Hf}_{0.7}\text{Ta}_{0.3})\text{C}/\text{SiC}$ bulk sample. a) Original BSE-SEM image, with a magnification of $1000\times$. b) Thresholding of the darkest contrast in (a) leads to the blue-marked pores in (b), and quantitative analysis via ImageJ gives the porosity value in area percentage (area%) as depicted in c). SEM-BSE image with a magnification of $10000\times$ in d) showing the microstructural region of the former powder particle with blue-marked micropores. The triangles show schematically the cross-sections of the nanoindenter.

schematically in the micrograph. They are depicted as triangle symbols with distances from $4\ \mu\text{m}$ to each other. The dependence of the cross-sections of the nanoindenter imprints and the presence of micropores will be rationalized later in the discussion in Section 3.2.6. The Archimedes drainage yielded a density of $3.442\ \text{g cm}^{-3}$ and an open porosity of 1.92%.

2.3.3. EPMA Results

Correlative elemental distribution maps obtained via the electron microprobe are shown in **Figure 7**. The SEM-BSE image in **Figure 7** depicts the analyzed region, where the former powder particles and the sinter necks are probed. Element distribution maps show enrichment of Si in the sinter necks, whereas Hf, Ta, and C are enriched at the internal surface regions of the former powder particles. This is consistent with SEM analysis, where increased grain sizes of TMCs are observed at the internal surfaces of the former powder particles. The oxygen and nitrogen distribution map shows no significant enrichment, which is in good agreement with the elemental analysis, as shown in Table 1. The elementary difference between the sinter necks and the former powder particles can be clearly seen in **Figure 7**. The pictorial resolution between SiC and TMCs in the former powder particles is not that clearly recognizable due to the relatively large beam diameter in the electron microprobe. The grain sizes of the TMCs are in the size range of the beam diameter (mostly $< 1\ \mu\text{m}$) and can, therefore, not be shown with EPMA in a well-resolved manner.

2.3.4. TEM

The collage of TEM images shown in **Figure 8** is composed of 253 individual TEM-BF images of a perforated, Ar^+ -ion-milled $(\text{Hf}_{0.7}\text{Ta}_{0.3})\text{C}/\text{SiC}$ bulk sample, combines a high magnification with a large field of view. Each TEM-BF image is taken with the smallest possible magnification of $5000\times$ to show the grain-like macrostructure composed of the former powder particles and the sinter necks. The image composition shows two distinct phases, namely, SiC and TMC, constituting the overall phase assemblage. SiC and $(\text{Hf}_{0.7}\text{Ta}_{0.3})\text{C}$ can easily be distinguished by their mass contrast in the TEM-BF images. As already described from OLM and SEM, also TEM imaging shows that the microstructure within the former powder particles is relatively

homogeneous. In contrast, the region of the sinter necks is heterogeneous regarding grain size, phase distribution, and grain morphology. The grain size distributions of TMCs in both microstructure regions are shown in the inset in **Figure 8** (blue = TMC grain size distribution of the former powder particles; red = TMC grain size distribution of the sinter necks). The area depicted within the white rectangle in **Figure 8** is shown more magnified in **Figure 9a**.

Figure 9 shows a more detailed contribution of the two microstructural regions. As depicted in **Figure 9b**, the former powder particle containing finely dispersed TMCs is embedded in a SiC matrix. The grain size distribution of SiC and TMC within the former powder particle is relatively homogeneous. The shape of the SiC particles within the former particles is ascribed as equiaxed, with SiC particle sizes ranging from 400 to 700 nm. In contrast, the TMC grains are slightly smaller in size, showing grain sizes ranging from 100 to 400 nm. Thus, the grain size distribution of both phases in the region of the sinter necks differs strongly. In general, SiC as well as TMCs shows increased grain sizes on the internal surfaces of the former powder particles. In particular, noticeable are the grain sizes of $(\text{Hf}_{0.7}\text{Ta}_{0.3})\text{C}$ with a maximum grain size measured of up to 800 nm, which means that the grain sizes near the internal surfaces are almost twice as large compared to the grain sizes in the former powder particles (cf. inset in **Figure 8**). Sinter necks mainly consist of large SiC crystals, with a maximum grain size measured up to $3\ \mu\text{m}$ (cf. **Figure 9d**).

Concerning the observed TMC particles formed upon crystallization during sintering, the EDS data are rather close to the overall composition of the single-source precursor (where Hf:Ta = 0.7:0.3). A mean Hf:Ta ratio of 0.74:0.26 (± 0.04) within the $(\text{Hf}_{0.7}\text{Ta}_{0.3})\text{C}$ grains was detected. This ratio was measured by analyzing 33 individual TMC particles via EDS point measurements. Therefore, the compositions of the respective crystallites of $(\text{Hf}_{0.7}\text{Ta}_{0.3})\text{C}$ are given in the molar ratios of the precursors within the text and the TEM images in **Figure 9** and **10**. EDS spectra of a TMC (depicted in blue) and SiC (depicted in green) are shown exemplarily in **Figure 9e**. EDS measurements do not indicate residual nitrogen within the TMC or SiC of the sintered sample.

Electron diffraction of SiC depicts the cubic phase (F-43 m, zinc-blende structure), which is also known as 3C-SiC or

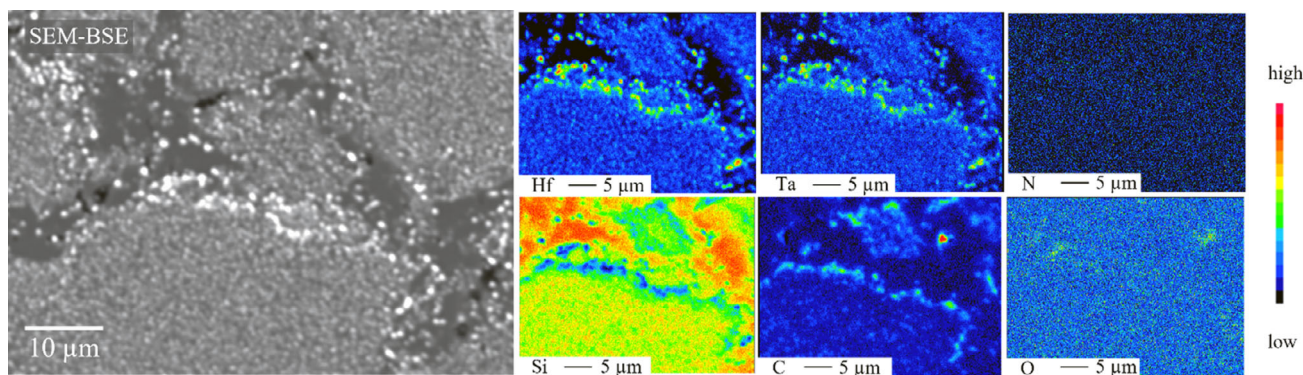


Figure 7. Cross-section of the sintered $(\text{Hf}_{0.7}\text{Ta}_{0.3})\text{C}/\text{SiC}$ bulk samples showing an SEM-BSE image and correlative EPMA element maps (Hf, Ta, N, Si, C, and O).

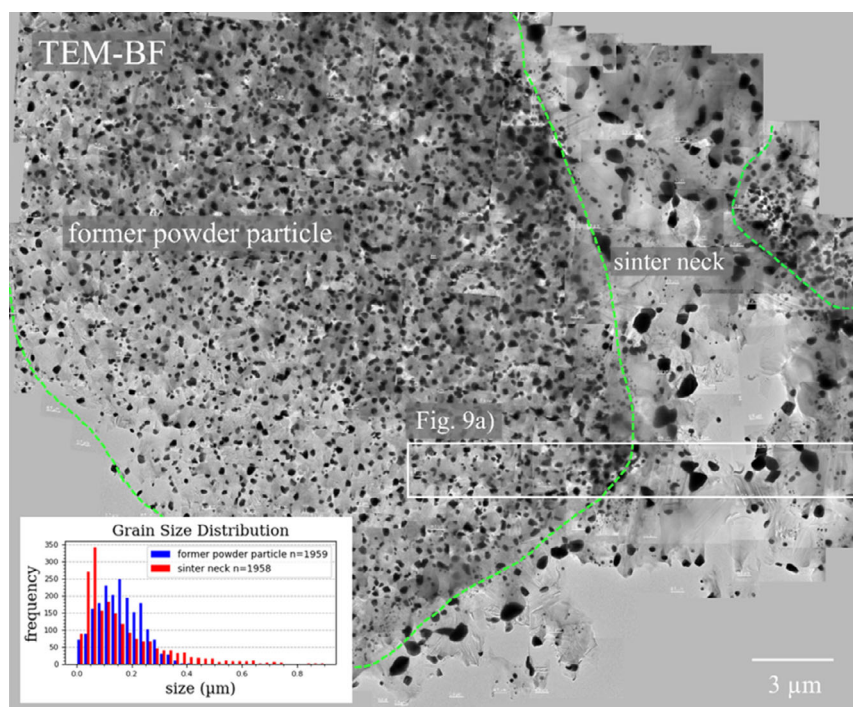


Figure 8. Numerous TEM-BF images assembled into one big picture showing the two main microstructural regions within the sintered $(\text{Hf}_{0.7}\text{Ta}_{0.3})\text{C}/\text{SiC}$ ceramic, namely, the former powder particle and the sinter neck. The image shows two former powder particles (center and upper right side are outlined with a dashed line) held together via the sinter neck, mainly consisting of large SiC grains. Inset shows the grain size distribution of the TMCs within the former powder particle as well as the sinter neck.

β -SiC. Often, twinned 3C-SiC grains are detected (cf. Figure 9d, f). At the imaging conditions near the $[110]$ zone axis, the SAED pattern of a SiC single-twin is shown in Figure 9f, where the $\langle 111 \rangle$ plane represents the twin boundary. In addition to single-twins, SiC exhibits SF in the sintered bulk sample. SFs, as shown in the HR-TEM image in Figure 10, show a sequence of bright/dark contrast. During TEM analysis, two polymorphs of SiC, namely, 3C-SiC and 6H-SiC were found (cf. SAED of Figure 10d,f). Also, the FAST sintered sample contains segregated (or “free”) carbon in the form of thin graphitic carbon layers/shells as is widely reported in the literature.^[34,63] The thickness of the carbon shell is highly dependent on the Hf content.^[5] However, the growth mechanism of the carbon is not fully understood yet.^[5,63]

2.3.5. Mechanical Properties in Nanoindentation

The three microstructural components (sinter necks, former powder particles, and porosity) present in the sintered material have been described in detail above and rationalize the use of the three components in the cf plots. Accordingly, the three-component fit yielded far better fitting results than a two-component fit (not shown here). The fit of three Gaussian-distributed components revealed the mechanical properties listed in Table 2. Figure 11a shows an optical light micrograph of the indentation array.

Maps of the measured properties are shown in Figure 11b. In this figure, each indent was attributed to one microstructure

component: blue for the low-hardness/low-modulus component, and yellow and red for the medium- and high-value component, respectively. From the maps in Figure 11b, in combination with the optical light micrograph, the correlation between mechanical properties and microstructure can be extracted: The former powder particles (containing SiC, $(\text{Hf}_{0.7}\text{Ta}_{0.3})\text{C}$ and nanopores) like the one in the center left and lower left in Figure 11b belong to the yellow component, showing medium hardness and modulus ($H = 27.3 \pm 3.3$ GPa; $E = 444 \pm 24$ GPa). Areas with macropores visible in the optical micrograph (for example, the large pore in the center left in Figure 11a) can be attributed to the blue component with low values ($H = 22.5 \pm 7.3$ GPa; $E = 367 \pm 78$ GPa). Sinter necks with no or little porosity of almost pure SiC belong to the red component with the highest values for hardness and modulus ($H = 36.7 \pm 2.9$ GPa; $E = 549 \pm 62$ GPa). This attribution also explains the large relative standard deviation of 33% and 21% for H and E , respectively, that was determined for the blue region (cf. Table 2; porous regions): As the blue component subsumes porous areas of the two actual components with varying porosity, no distinct material properties were identified in the cf. The surface calibration was performed at the lower part of the area, thus a constant to calibrate the frame stiffness is determined and assumed for the whole indentation region. However, due to a tilted sample surface and the large area, the assumed frame stiffness calibration cannot precisely describe the entire indentation array and causes an additional scatter on the hardness values, especially the modulus values on the top right corner.

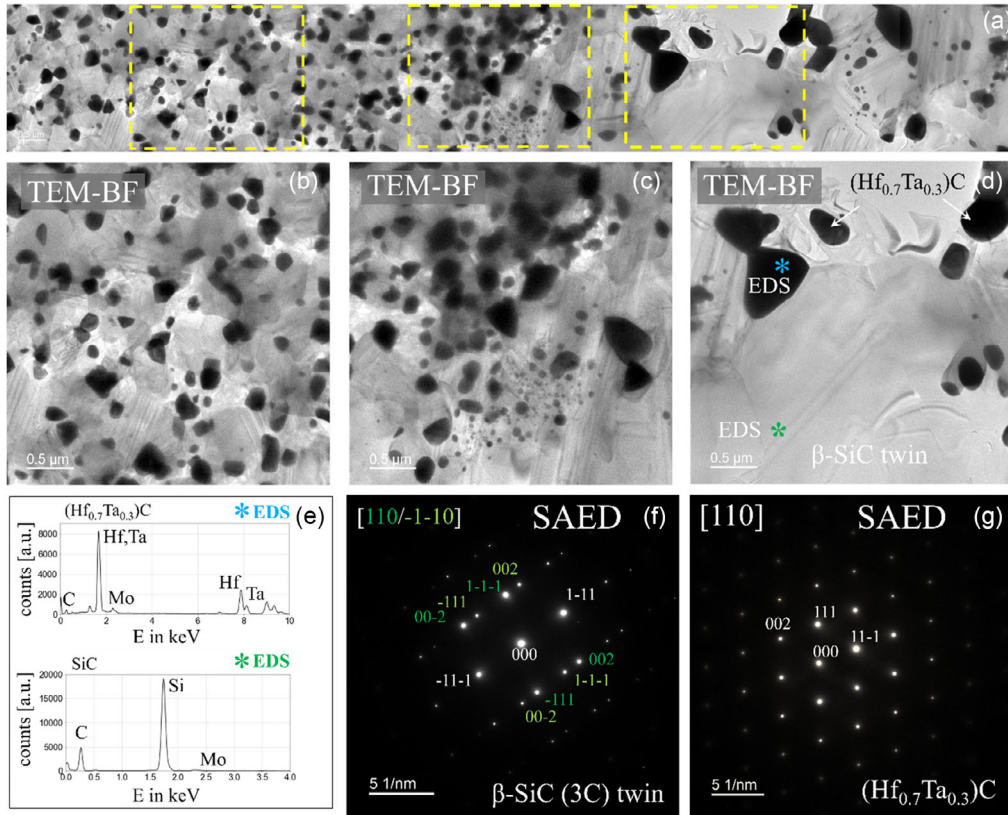


Figure 9. a–d) TEM-BF images, e) EDS spectra of TMC and SiC, and f,g) SAED pattern of the constituting phases SiC and TMC within the dense $(\text{Hf}_{0.7}\text{Ta}_{0.3})\text{C}/\text{SiC}$ ceramic.

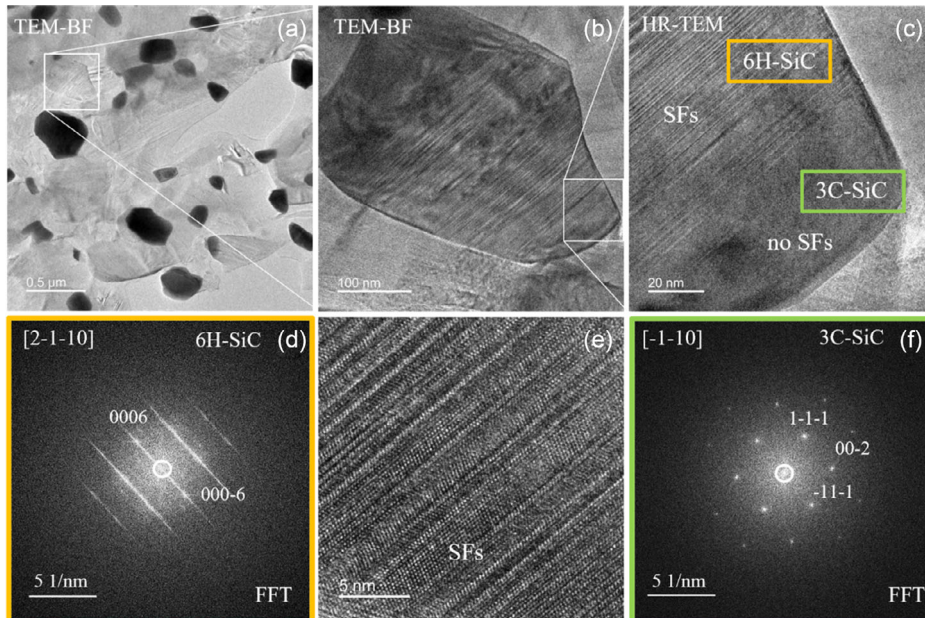


Figure 10. TEM images of 3C-SiC (green) and 6H-SiC (orange) with SF in SiC. a,b) TEM-BF images; c,e) HR-TEM images; d,f) corresponding FFT images of 6H-SiC (orange) and 3C-SiC (green).

Table 2. Mechanical properties of the three microstructural components within the $(\text{Hf}_{0.7}\text{Ta}_{0.3})\text{C}/\text{SiC}$ ceramic in comparison to similar ceramic materials published in literature. Although no Vickers hardness testing was performed here, values from the literature are shown for comparison.

| Material | Processing route | Consolidation | FAST parameter | Vickers hardness [GPa] | Nanohardness [GPa] | Elastic modulus [GPa] | References |
|---|------------------|---------------|--|------------------------|--------------------|-----------------------|------------|
| | | | sinter temperature in °C/pressure in MPa/dwell time in min | | | | |
| Former powder particle (TMC + SiC + micropores) | PDC | FAST | 2200/50/20 | – | 27.3 ± 3.3 | 444 ± 24 | This work |
| SiC/HfC | PDC | FAST | 2200/50/20 | – | 25.6 ± 4.9 | 324.5 ± 47.6 | [91] |
| TaC/SiC | PM | FAST | 1900/40/5 | 21.0 ± 10 | – | 498 ± 10 | [10] |
| HfC + MoSi ₂ | PM | FAST | 1900/100/15 | 19-21 | 26-28 | 450-500 | [92] |
| Sinter necks (mainly SiC) | PDC | FAST | 2200/50/20 | – | 36.7 ± 2.9 | 549 ± 62 | This work |
| SiC/C | PDC | FAST | 2200/50/20 | – | 24 ± 3 | 309 ± 29 | [95] |
| SiC | PM | FAST | 2050/69/10 | 32 ± 0.7 | – | 440 ± 20 | [96] |
| SiC | Single crystal | – | – | – | 41.0 ± 1.2 | 549 ± 20.6 | [97] |
| Porous + topographically-affected regions | PDC | FAST | 2200/50/20 | – | 22.5 ± 7.3 | 367 ± 78 | This work |

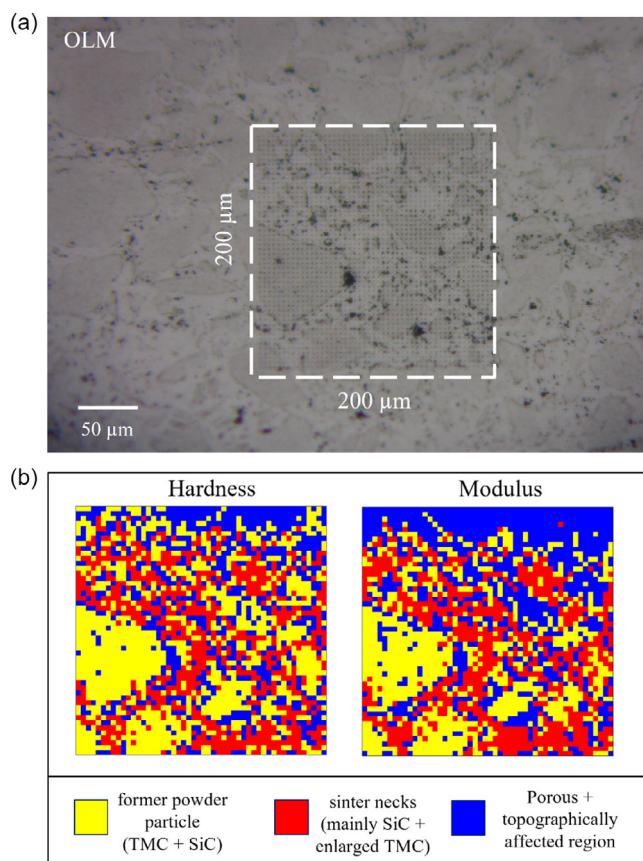


Figure 11. a) Optical light micrograph showing the nanoindentation array of 50×50 indents. b) Hardness and modulus maps of the area indented in (a). Based on the detected mechanical properties, each indent was attributed to one of the identified microstructural components: blue for the porous regions, yellow for the former powder particles, and red for the sinter necks. The scatter in the upper part of the map is more pronounced due to the tilted sample surface.

The maps in Figure 11b show relatively low values for H and E at the top edge of the maps. Correspondingly, the areas were predominantly attributed to the blue component in c), although powder particles can be discerned in the optical micrograph. The low values of hardness and modulus in this blue area can be explained by the porosity underneath the surface, which is not visible in the optical micrograph. Due to the potentially different microstructures in the subsurface, the mechanical properties determined by nanoindentation are not necessarily correlated to the microstructural components identified by the surface characterization.

3. Discussion

3.1. Discussion Regarding the as-Pyrolyzed 1000 °C Powders

As shown in Figure 4, nanocrystalline TMCs with grain sizes from ≈ 5 nm up to 100 nm were found in the mostly amorphous as-pyrolyzed $\text{Si}(\text{Hf}_{0.7}\text{Ta}_{0.3})\text{C}(\text{N},\text{O})$ ceramic synthesized via the PDC route. Thus, after pyrolysis, the X-ray amorphous powders (cf. Figure 2) already depict a not completely homogeneous microstructure and tend to undergo local early crystallization. This behavior has been previously reported in refs. [31,46]. The Hf:Ta ratios of the early crystallized TMCs were found to be 0.2:0.8 instead of the anticipated Hf:Ta ratio of 0.7:0.3. An explanation for the described Hf:Ta ratio could be the wide two-phase region in the HfC-TaC phase diagram at low temperatures (phase diagram can be found in ref. [46]). According to the binary phase diagram, Hf-rich TMCs should also be thermodynamically stable. However, due to local TEM measurements, it is possible that the Hf-rich precipitates were not sampled here. Moreover, it should be considered that the system does not consist of only three elements (Hf, Ta, C) but contains also small amounts of N and O. Thus, other phases could also occur in the higher-level phase diagram.

3.2. Discussion Regarding the Microstructural Evolution Within the FAST-Sintered Bulk Samples

Several microstructural characteristics have been observed through *ex situ* microscopic analyses on the dense (Hf_{0.7}Ta_{0.3})C/SiC ceramic. These characteristics include crystallization via phase separation from a mostly amorphous Si(Hf_{0.7}Ta_{0.3})C(N,O) into a crystalline (Hf_{0.7}Ta_{0.3})C/SiC ceramic, the consolidation of initial powder particles via matter transfer mechanisms resulting in neck formation, increased grain sizes of TMCs at the internal surfaces of former powder particles, multitwinning (SF) in SiC, and entrapped residual closed porosity.

FAST used as the consolidation method is an under-pressure technique.^[17,48,51,64] Further, a pulsed direct current is applied additionally to the external heating of the die.^[17,64] The combination of the sinter parameters (mechanical, thermal, and electrical effects) gives rise to several mechanisms like densification mechanisms, Joule heating, thermal gradients, percolation effects, Peltier effect, electromigration, and/or electrochemical reduction, diffusion processes^[51,64,65] all contributing to the microstructural evolution observed in the studied (Hf_{0.7}Ta_{0.3})C/SiC PDC.

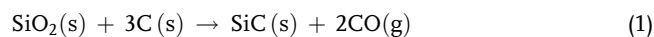
The evolution of the final microstructure is not exclusively dependent on the sintering parameters.^[34] It also depends on the powder particle size distribution of the starting powder (influenced by ball milling and sieving). In addition, the final microstructure after consolidation depends strongly on the chemistry of the starting powder.^[1,34] The chemical reactions (decomposition, phase separation, crystallization, and formation of gaseous species) occurring during the FAST process also affect the final microstructure of the PDC. In the following sections, the impact of the different processing parameters on the microstructure and chemistry of the (Hf_{0.7}Ta_{0.3})C/SiC is discussed.

3.2.1. Role of Atmosphere/Gaseous Species Influencing the Evolving Microstructure

While the initial starting powder consists of a mostly amorphous Si(Hf_{0.7}Ta_{0.3})C(N,O) glass network, it undergoes crystallization reaction, phase transitions, vaporization, or condensation reactions (influencing again the sinter behavior of the system). Particularly in the PDC systems, thermal decomposition reactions lead to local chemical differences during the sintering process.^[46,66,67] In general, the microstructural evolution of amorphous polymer-derived ceramics due to FAST/SPS includes many processes/reaction steps, which are not well understood yet. Some of the crucial subreactions were described recently in literature in the refs. [68–70]. For example, a phase separation from amorphous SiCO ceramics into SiO₂, SiC, and C starts at and above 1300 °C.^[70,71]

Thus, the occurrence of various subreactions is also assumed for the transition from the amorphous Si(Hf_{0.7}Ta_{0.3})C(N,O) to the crystalline (Hf_{0.7}Ta_{0.3})C/SiC ceramic. EDS point measurements utilized in SEM and TEM clearly show the presence of oxygen and nitrogen in the as-pyrolyzed Si(Hf_{0.7}Ta_{0.3})C(N,O) ceramics via the corresponding element peaks in the EDS spectra (cf. Figure 3b and 4d). In accordance with EDS analyses, measurements via hot gas carrier extraction led to an oxygen content

of ≈4 wt% for the as-pyrolyzed Si(Hf_{0.7}Ta_{0.3})C(N,O) (compared with elemental analysis, Table 1). The oxygen content after the consolidation via FAST was determined to be <0.2 wt%, indicating a mass loss of oxygen during the sintering. Based on these observations, it is assumed that the decreased oxygen content in the sintered ceramics can be ascribed to the carbothermal reduction reaction between silica and carbon resulting in SiC and CO, given by (Equation (1))^[68]:



If this reduction reaction (Equation (1)) takes place within the Si(Hf_{0.7}Ta_{0.3})C(N,O) system during consolidation, even only to a minor extent, it may affect the sintering behavior due to the formation of the gaseous species of CO, as it is known that the atmosphere plays a crucial role during densification.^[51] However, neither silica was found in the analytical measurements via XRD nor in TEM.

A nitrogen content of 3.64 wt% was detected for the as-pyrolyzed Si(Hf_{0.7}Ta_{0.3})C(N,O) PDCs (cf. Table 1), whereas the nitrogen content in the sintered (Hf_{0.7}Ta_{0.3})C/SiC ceramic was only 0.31 wt%, also indicating a mass loss during the sintering process. These results agree with the results from Wen et al. where the authors also stated a relative mass loss with respect to the as-pyrolyzed and subsequently annealed ceramics due to carbothermal reactions taking place.^[5] This raises the question of to what extent or even if the gaseous nitrogen plays a role in the sintering process. As no nitrogen was detected via EDS in the constituent phases of SiC and TMCs in the sintered sample (cf. Figure 9e), it is also reasonable that gaseous nitrogen is formed during the sintering process, which is then entrapped in closed pores and thus prevents complete densification.^[51] In conclusion, the evaporation of material, the carbothermal reduction reactions, and the development of gaseous species in the Si(Hf_{0.7}Ta_{0.3})C(N,O) polymer-derived ceramic are very likely.

3.2.2. Influence of Sinter Additives on the Sintering Behavior of SiC

In Section 2.3, the microstructure of the dense (Hf_{0.7}Ta_{0.3})C/SiC ceramic is described in detail. Especially the detection of sinter necks consisting of large SiC grains raises the question of how these microstructures evolve during the sinter process via SPS/FAST. Sintering aids (such as Y₃Al₅O₁₂ compound or alumina) could lower the sintering temperature, enhance the densification rate, and slow down the grain growth kinetics, as reported by Maitre et al.^[72] This was already shown by studies from Stobierski and Gubernat, where the effect of carbon and boron on the sintering behavior of SiC was studied separately.^[73,74]

Additives of carbon seem to block the mass transport processes and prevent grain growth of SiC.^[74]

The incorporated transition-metal complexes within the here-studied (Hf_{0.7}Ta_{0.3})C/SiC may also influence the phase formation and sintering behavior of SiC via catalytic effects. Recently, Rau et al. reported that transition metal fillers reduce the formation temperature of SiC through the generation of TMCs, silicides, and oxides.^[75] Previous studies also showed that metals such as Fe influence the crystallization temperature of

β -SiC via catalytic effects.^[75] According to Rau et al. SiC formation is already possible at temperatures around 1300 °C, primarily because of Fe, which locally reduces the energetic barrier for β -SiC crystallization.^[75] These studies suggest a similar influence of the transition metals Hf and Ta on the formation temperature of SiC. Further research is needed here.

3.2.3. Influence of Mechanical Effects on Microstructure

TEM investigations show the occurrence of SiC single-twins and SF (Figure 10). Polytypism in SiC is a well-known crystallographic property that describes the stacking of structural cubic modules, which was found to be intimately connected to twin and SF.^[76,77] For the cubic 3C-SiC (β -SiC) with its space group F-43m (zinc blende structure), the addition of fully ordered cubic twinned modules leads to the noncentrosymmetric space group P6₃mc, which is indicated as 6H-SiC (hexagonal or α -SiC).^[77] Therefore, the addition of the twinned modulus leads to a reduction in the overall symmetry. Interestingly, mostly 3C-SiC is found in the XRD pattern (cf. Figure 2), whereas TEM imaging clearly indicated the appearance of 6H-SiC, depicted by the bright/dark (B/D) contrast (cf. Figure 10), which is a result of dynamical diffraction.^[77] The B/D contrast emerges by slightly tilting the crystal away from the Bragg condition.^[77] The contrast is intensified along the polytype-sensitive rows, which in 6H-SiC is the [11–20] zone axis. Literature also indicates that indexing the XRD pattern to define the polytype of SiC is not straightforward in many cases.^[78] Several studies have reported a very weak diffraction peak at 34.2° in the XRD pattern of 3C-SiC,^[78–80] which is assigned to the <10–11> plane of the 6H-SiC. Unfortunately, this weak diffraction peak in the XRD pattern in Figure 2 is superimposed by the (111) peak of the (Hf_{0.7}Ta_{0.3})C, lying at 34.8°.

It cannot be conclusively stated, whether twin boundaries in SiC are formed during the phase transformation and the induced change in the crystal structure from α -SiC to β -SiC due to cooling or via deformation induced by mechanical load during the sintering process.^[81]

3.2.4. Influence of Electrical Currents on the Microstructure

As the literature describes, high-electric currents flow directly through the green body, where interactions between the electric current and the material will occur.^[51] Indeed, the green body is not entirely dense, meaning the electric current does not flow evenly through the material.^[51] Thus, there will be a network of percolation current pathways forming, which then give rise to an increased Joule heating along those pathways.^[51]

The observed microstructure of the (Hf_{0.7}Ta_{0.3})C/SiC, as shown in Figure 5f, may result from such percolation current pathways. They are expected to occur especially in the contact regions of the former powder particles, where sinter necks and grain-coarsened TMCs are observed. Figure 5f exhibits several regions showing pearl-like structures consisting of TMCs, which may indeed be regions, where the pulsed direct current and intense local Joule heating have engendered the formation of such distinctive pearl structures. Interestingly, there is a general increase in the grain size of the TMC at or near the internal

surfaces of the former powder particles (cf. Figure 8), which could be explained by the pulsed direct current flowing along the grain boundaries. The binary carbides HfC, TaC, and their solid solutions (Hf_xTa_{1-x})C possess a mixture of metallic, covalent, and ionic bonding; whereas the metallic character gives rise to high thermal conductivity (heat conductivity) and high electrical conductivity.^[3,5,11,33,82] The thermal conductivity of TMCs shows several unusual characteristics.^[83] For ordinary crystalline solids, it is not expected that the thermal and electrical conductivity increase with increasing temperature, as it is described for TMCs.^[11,82–84] The pulsed electric current used within the FAST will induce additional temperature, causing a further increase in the sample temperature and thus is expected to influence the grain growth of TMCs on internal surfaces (cf. grain sizes of TMCs inside former powder particles vs grain sizes of TMCs on the internal surface of former powder particles in Figure 8). Furthermore, the pulsed current gives rise to local higher temperatures due to the Joule heating effect,^[7,17,48,61] which may lead to an increased matter transport due to enhanced diffusion coefficients and thereby may also lead to additional grain growth of TMCs, as shown in the schematic drawing in Figure 12.^[3,51,85,86] That the current plays an intrinsic role on the mass transport contributing to the formation of distinct microstructures has already been described for materials, such as metallic glasses^[86] and ceramic materials.^[50]

3.2.5. Processes Influencing the Grain Size During Sintering

The microstructure of the (Hf_{0.7}Ta_{0.3})C/SiC ceramic shows in general two different grain size distributions (cf. Figure 8). The grain sizes of both phases within the former powder particle (SiC and TMC) are much smaller than their respective grain sizes within the sinter necks. A possible reason for the smaller grain sizes in the former particles could be the presence of micropores at grain boundaries, as shown in Figure 5 and 6d. Further, exaggerated grain growth of SiC and TMC in the microstructural region of the former powder particles is avoided due to the pinning effect of the secondary phase. Similar observations of grain growth stagnation due to pinning effects were reported for several ceramics processed via FAST/SPS, such as nanocrystalline yttria,^[87] B₄C-TiB₂ composites,^[88] or TaC/SiC composites.^[10]

Grain sizes of SiC within the sinter necks are larger by a factor of two as compared to the grain sizes within the microstructure of the former powder particles, as can be seen in Figure 8. As described by Guillon et al.^[51] the Peltier effect plays a crucial role in densification. Especially as semiconductor materials such as SiC have much higher Peltier coefficients than metals or graphite, resulting in considerable Peltier heating, which can then reach up to 10 % of the total heating power delivered by the process.^[51]

Another explanation for increased SiC grain sizes in the sinter necks could be that a combination of high temperatures and further enlarged “free” space in the particle-to-particle contact zones is available. In addition, oxygen impurities in the starting powder (cf. EDS spectrum in Figure 3b and elemental analysis in Table 1) will also favor exaggerated grain growth when evaporation–condensation mechanisms become active at high temperatures.^[51] Thus, the slightly increased oxygen content is supposed

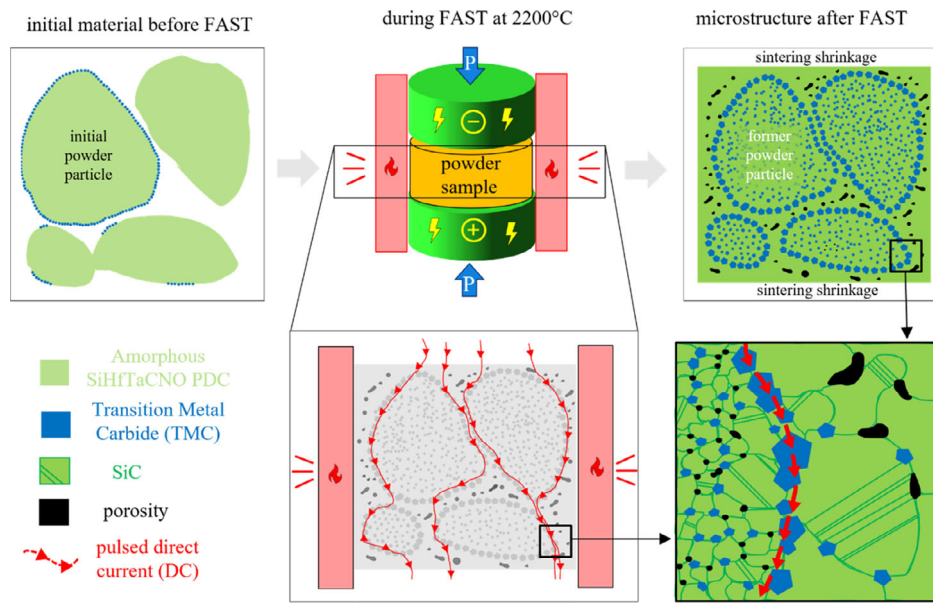


Figure 12. Schematic drawing of the microstructure evolution starting from the initial powder consisting of mostly amorphous $\text{Si}(\text{Hf}_{0.7}\text{Ta}_{0.3})\text{C}(\text{N},\text{O})$ and the microstructure of the $(\text{Hf}_{0.7}\text{Ta}_{0.3})\text{C}/\text{SiC}$ ceramic during and after the FAST process respectively.

to influence the particle size of the TMCs located on the internal surfaces of the former powder particle, as it was already shown in our previous study.^[46] In general, it is well-known from literature that the sintering of nonoxide ceramics is challenging due to oxygen impurities promoting coarsening phenomena.^[10,19,46,89] It is assumed in literature that oxygen-containing impurities enhance the evaporation/condensation kinetics leading to an increased grain growth of TMCs.^[89] Alternatively, we speculate that oxygen increases the distance between the matrix atoms and thereby enhances the diffusion of the TMs. However, a fundamental explanation of this effect is still missing.

3.2.6. Discussion of the Mechanical Properties via Nanoindentation Tests

Following the microstructural description, the former powder particles (yellow component in Figure 11) are expected to show the highest H values, as a result of the precipitation hardening of the secondary phase (TMCs in SiC matrix). The mechanical properties derived from the indentation of SiC and TMCs take into account the presence of a variety of nanopores present in the former powder particles (cf. SEM-BSE images in Figure 5e and 6d). Thus, there is a high probability that the Berkovich indenter tip (assuming a cross-sectional area of $\approx 2 \mu\text{m}^2$) would also indent regions, in which nanopores are present. This is clearly shown with the schematic drawing of the cross-section of the indenter in Figure 6d according to the so-called grid indentation technique reported in ref. [90].

In general, studies on the mechanical properties of FAST-processed PDCs containing SiC and TMCs are still scarce in the literature. For reference, Table 2 shows a comparison of the mechanical properties of ceramic composites synthesized via the PDC or the PM route and consolidated via FAST.

Nanoindentation yielded results for H and E in the former powder particles (yellow component in Figure 11b) similar to literature values of comparable ceramic composites. The value of Young's modulus, $E = 444 \pm 24 \text{ GPa}$, falls in between the values obtained for HfC/SiC ($E = 324 \text{ GPa}$ in ref. [91]) and TaC/SiC ($E = 498 \text{ GPa}$, in ref. [10]), as is expected for intermediate compositions.

The SiC/HfC sample published in ref.[91] was also prepared via the PDC route using the same FAST parameters ($2200 \text{ }^\circ\text{C}/50 \text{ MPa}/20 \text{ min}$). According to the authors, the H and E data were determined by the mean value of 100 indents, without a microstructural differentiation.

Another comparison listed by Sciti et al.^[92] contains mostly HfC and only small amounts of silicides, resulting in a very different microstructure compared to the herein-studied ceramic.

High load indentation hardness (max. load 1 N, not shown here) suggests a value range comparable to refs. [93,94]. However, the scatter is large in our sample because of the presence of pores. This differs from the results of TMCs prepared by other sintering routes (such as high-pressure sintering or hot pressing).^[93,94] The sinter necks (red component in Figure 11) show the highest measured values of H and E in the $(\text{Hf}_{0.7}\text{Ta}_{0.3})\text{C}/\text{SiC}$ ceramic. The nanoindentation results are listed with other literature data in Table 2.

In terms of the synthesis and processing (PDC route and FAST process), the mechanical properties of the sinter necks were expected to be very similar to the values listed in ref. [95]. Nevertheless, the mechanical properties E and H of the SiC-containing sinter neck examined here, show significantly higher values compared to the SiC/C ceramic in ref. [95]. By contrast, the mechanical properties of FAST-sintered SiC reported by Hayun et al.^[96] are closer to the values in this study. The authors described dense ($\text{RD} = 99.4\%$) FAST-processed covalent SiC ceramics containing E -modulus of $\approx 440 \pm 20 \text{ GPa}$ and hardness

of 32 ± 0.7 GPa. However, the mechanical properties of the sinter necks are most comparable to those of the SiC single crystals, published by Datye et al.^[97] As can be seen from Figure 5e, the sinter necks are very dense. Also, grain sizes of SiC in the sinter necks are relatively large, reaching grain sizes up to $3 \mu\text{m}$, which is larger than the individual indents. This leads to nanoindentation results similar to single crystal data. The few pores detected in the sinter necks are large, at least of similar size compared to the indenter (cf. Figure 5e). Thus, any indented pores are identified as porous regions (blue component) and do not contribute to the properties identified for the sinter necks.

In summary, the comparison in Table 2 shows that the mechanical properties of the sinter necks in the $(\text{Hf}_{0.7}\text{Ta}_{0.3})\text{C}/\text{SiC}$ PDC reveal the highest values of E and H among the published literature, being closer to single crystal properties. In addition, it demonstrates that the mechanical properties measured via high-throughput nanoindentation can be correlated to different microstructural regions, when a heterogeneous microstructure is present.

4. Conclusion

Microstructural evolution starting from as-pyrolyzed PDC powders and thereof consolidated dense $(\text{Hf}_{0.7}\text{Ta}_{0.3})\text{C}/\text{SiC}$ was examined in detail using various microscopy methods and nanoindentation. The microstructure of the bulk ceramic after sintering contains three different microstructural regions, consisting of the former powder particles, sinter necks, and some residual porosity. It was observed that internal surfaces are in particular microstructural regions where large TMCs are present due to increased diffusion facilitated by several sintering parameters as well as the presence of oxygen facilitating grain growth. Further, the microstructural evolution of PDCs upon FAST is certainly influenced by numerous effects, such as thermal, electrical, and mechanical mechanisms. Joule heating triggered by the pulsed electric current, flows along grain boundaries of former powder particles, influencing the grain growth of TMCs and therefore contributing to an inhomogeneous microstructure development of the $(\text{Hf}_{0.7}\text{Ta}_{0.3})\text{C}/\text{SiC}$ ceramic. Exaggerated grain growth of TMCs within the former powder particle is prevented due to the pinning effect of the secondary phase of SiC and the presence of nanopores. In addition to a detailed microstructure characterization of the anticipated bulk ceramics, it was shown that high-throughput nanoindentation on polymer-derived bulk ceramics is an effective method to identify mechanical properties and correlate those to microstructural components. The comparison of optical micrographs and property maps supports these correlations. Sample porosity impacts the statistical analysis of nanoindentation significantly. Its influence needs to be considered for the number of components fitted and the interpretation of mechanical properties.

5. Experimental Section

Materials Synthesis via the PDC Route: The detailed synthesis of the single-source precursors and the preparation of dense bulk samples via FAST in the $\text{Si}(\text{Hf,Ta})\text{C}$ system can be found in detail in refs. [5,36,53]. However, a short processing overview of the materials is given below.

The $\text{Si}(\text{Hf}_x\text{Ta}_{1-x})\text{C}(\text{N,O})$ ceramic powders were synthesized via the single-source precursor route using the standard Schlenk technique. The polymeric precursor used is a commercially available allyl-hydrido-polycarbosilane (SMP-10, Starfire, System Inc., USA) with a theoretical molecular formula of $[\text{SiH}(\text{CH}_2\text{CH}=\text{CH}_2)\text{CH}_2]_{0.1n}[\text{SiH}_2\text{CH}_2]_{0.9n}$. The metal amino complex used for the incorporation of Hf is tetrakis(diethylamino)hafnium, also known as TDEAH or $[(\text{Me}_3)_2\text{N}]_4\text{Hf}$, (CAS no: 19 824-55-6, Sigma-Aldrich Chemie GmbH, Taufkirchen, Germany). For the incorporation of Ta, the pentakis(dimethylamino)tantalum(V), also known as PDMAT or $\text{Ta}(\text{NMe}_2)_5$ (CAS no: 19 824-59-0, Sigma-Aldrich Chemie GmbH, Taufkirchen, Germany) was used. Two PDCs with different Hf:Ta molar ratios were fabricated, one with a higher Hf content, and another with a higher Ta content. The molar ratios of the metal complexes of the Hf to Ta ratios were set to 1:4 for the Ta-rich $(\text{Hf}_{0.2}\text{Ta}_{0.8})$ and 7:3 for the Hf-rich samples $(\text{Hf}_{0.7}\text{Ta}_{0.3})$. The metal amino complex to polymer molar ratio (TDEAH + PDMAT:SMP10) was set to 3:7 for both compositions. For the Hf-rich composition, SMP10 (3 g), PDMAT (0.375 g), and TDEAH (1.018 g) were used. The synthesized single-source precursors were pyrolyzed in an Ar^+ atmosphere at 1000°C to prepare the ceramic starting powders.

Densification via FAST/SPS: The as-pyrolyzed ceramic powders were milled using a clean agate pestle and mortar, sieved to a grain size of less than $100 \mu\text{m}$ composing the initial material for the consolidation process. The powder was inserted into a graphite die with an inner diameter of 20 mm. The die was covered with graphite foil, reducing damage to the punch surface and facilitating sample removal after the FAST process. The die was placed into an FCT HP D 25/1 FAST/SPS apparatus (FCT Systeme GmbH, Frankenblick, Germany) and consolidation was conducted at 2200°C under vacuum, a uniaxial pressure of 50 MPa and a dwell time of 20 min. The heating rate was 100K min^{-1} up to 2200°C , the cooling rate was set to 220K min^{-1} until RT was reached. A pulsed electric current was applied with a pulse duration of 25 ms and a pause time of 5 ms throughout the experiment to increase the temperature in a controlled way. The temperature was measured with an optical pyrometer. The samples obtained after pyrolysis and sintering will be denoted $\text{Si}(\text{Hf}_x\text{Ta}_{1-x})\text{C}(\text{N,O})$ for the as-pyrolyzed powders and $(\text{Hf}_x\text{Ta}_{1-x})\text{C}/\text{SiC}$ for the dense bulk samples.

Materials Characterization: Chemical Composition and Phase Composition: Elemental analysis of as-pyrolyzed and FAST-sintered bulk samples was performed at Mikroanalytisches Labor Pascher (Remagen, Germany). As-pyrolyzed powder samples were not additionally pulverized for elemental analysis, whereas the FAST-sintered bulk samples were pulverized with a tungsten carbide (WC) grinder. The Hf, Ta, and Si contents were determined using inductively coupled plasma atomic emission spectrometry. The nitrogen and oxygen contents were measured by hot gas carrier extraction. The carbon content of the ceramics was determined via combustion analysis.

The phase composition and crystallinity of the as-pyrolyzed and sintered bulk samples were analyzed by X-ray diffraction (XRD) analysis using a D8 Advance X-ray diffractometer (Bruker Corporation, Billerica, USA), using Ni-filtered $\text{Cu-K}\alpha$ radiation ($\lambda = 1.5406 \text{ \AA}$). The step size was set to 0.015° with 15 s per step in the measurement range from $2\theta = 15^\circ$ to 100° . The baseline correction was performed by using the Match! Software (Crystal Impact – Dr. H. Putz & Dr. K. Brandenburg GbR, Bonn, Germany). Diffraction peaks were indexed using the International Centre for Diffraction Data (ICDD) Powder Diffraction File (PDF) database.^[98]

Materials Characterization: Optical Light and Electron Microscopy: Scanning electron microscopy (SEM) was performed on a JSM-7600F (JEOL Ltd, Tokyo, Japan) equipped with an X-Max energy-dispersive X-ray spectroscopy (EDS) detector (Oxford Instruments, Abingdon, UK). SEM was used to gain chemical information via backscatter electron imaging (SEM-BSE) and surface structure information via secondary electron imaging (SEM-SE). The accelerating voltage for SE and BSE imaging as well as for EDS was set to 15 keV, using a beam diameter of max. 2 nm and a working distance of 8 mm. The acquisition time for each EDS point measurement was 30 s, and the estimated relative error was $\approx 5\%$. SEM analysis of the as-pyrolyzed powder sample was conducted

on ground powder particles placed on an adhesive carbon pad (Plano GmbH, Wetzlar, Germany). For SEM and electron probe microanalysis (EPMA) of the sintered bulk samples, cross-sections were cut using a slow-speed ISOMET diamond saw (Buehler, Leinfelden-Echterdingen, Germany). Samples were ground and polished using a MultiPrep tripod polisher (Allied HighTech Products Inc., California, USA) with diamond lapping film disks (15, 9, 6, 3, 1 μm).

EPMA analysis was carried out using a JXA-8100 microprobe (JEOL Ltd, Tokyo, Japan) equipped with five wavelength-dispersive X-ray spectrometers to gain chemical information via semiquantitative elemental distribution maps. EPMA was performed using an accelerating voltage of 15 keV, a dwell time of 30 ms per pixel, and a probe current of 30 nA with a maximum beam diameter of $<1 \mu\text{m}$. For obtaining the element maps, the following standards were used: Fe_4N (as standard for N), Cr_3C_2 (as standard for C), Al_2O_3 (as standard for O), Si, Hf, and Ta.

Transmission electron microscopy (TEM) studies were conducted on a JEM-2100 microscope (JEOL Ltd, Tokyo, Japan) operated at an acceleration voltage of 200 keV, equipped with a charge-coupled device camera and a beryllium double-tilt holder for sample orientation, while EDS spectra were conducted with an X-Max EDS detector (Oxford Instruments, Abingdon, UK). TEM bright-field imaging (TEM-BF) and high-resolution TEM imaging (HR-TEM) in combination with the selected area electron diffraction (SAED) technique were carried out to investigate the microstructure and gain crystallographic information of the containing phases.

TEM studies of as-pyrolyzed powders were conducted on ground powder samples. Therefore, powders were mechanically pulverized using a clean agate pestle and mortar, ultra-sonicated in ethanol, and pipetted on a gold carbon-lacy grid (Plano GmbH, Wetzlar, Germany). To distinguish between Hf and Ta, TEM gold grids were used instead of standard copper grids since a peak overlap between the L_{α} lines of the transition metals (L_{α} Hf = 7.889 keV, L_{α} Ta = 8.146 keV) with the K_{α} line of Cu = 8.046 keV exists, while the L_{α} line of Au at 9.713 keV shows no overlap. TEM-foil preparation followed the standard ceramographic preparation technique as described above for SEM and EPMA measurements. A thin plan parallel TEM foil with a maximum thickness of 15 μm was glued onto a TEM grid. The final thinning process to achieve electron transparency was conducted via Ar^+ -ion milling on a precision Duomill 600DIF (Gatan Inc, California, US) at an accelerating voltage of 4 keV until perforation is obtained. The as-prepared TEM powder and bulk samples were carbon-coated to avoid sample charging under the incident electron beam for SEM, TEM, and EPMA investigations.

Materials Characterization: Porosity via Quantitative Image Analysis and Archimedes Method: Information regarding the closed porosity of dense bulk samples rely on SEM-BSE images of polished surfaces, which were interpreted via quantitative image analysis using the software package of ImageJ (National Institute of Health, USA).^[99] The area percentage (area%) of the closed porosity (skeletal porosity) was calculated on SEM-BSE images with a magnification of 500 \times and 1000 \times . Within the magnification of 1000 \times , both microstructural regions (former powder particles and sinter necks) are depicted, preventing an overestimation of one or another microstructural region.^[100] Images that are 1000 \times magnified show a representative distribution of pores, whereas images with a magnification of 500 \times do not reveal the pore information.

Digital image analysis was used to estimate the mean 2D porosity via thresholding. SEM-BSE images were converted into the 8-bit format, which constitutes 256 different grayscale intensities. The range of the gray intensities in every image varies from 0 to 255, with 0 corresponding to black and 255 to white. Pores appear in different black or dark gray shades in the BSE images due to the atomic number sensitivity of the backscattered electron imaging. They can be identified because the contrast between pores and the containing solid phases is sufficient to be quantified by image analysis.^[101,102] To further confirm the density and open porosity of the monolithic sample, the Archimedes method was used.

Mechanical Properties: The monolithic bulk samples for the nanoindentation tests were cut into small blocks, followed by a standard ceramographic preparation as described in Section 5 Materials Characterization: Optical Light and Electron Microscopy. The ceramic blocks were glued onto standard aluminum dies using crystal bond.

The samples were investigated using the InForce50 actuator in a G200X Nanoindenter (KLA-Tencor, Milpitas, California USA) equipped with a diamond Berkovich tip. 2500 indents were made using the NanoBlitz mapping tool, arranged in a 50 \times 50 array with a spacing of 4 μm between the indents. Considering an indentation depth of 300–400 nm, a mutual influence of neighboring plastic deformation zones can thus be neglected.^[103] Thus, the total surface area probed was 200 \times 200 μm^2 . The nanoindentation experiments were performed at a strain rate of 0.2 s^{-1} to a maximum load of 50 mN. The quasi-static load–displacement data were analyzed using the built-in software package based on the Oliver–Pharr method, assuming a Poisson ratio $\nu = 0.2$ for the sample,^[104] and for the indenter tip an elastic modulus and Poisson ratio of 1141 GPa and 0.07, respectively. Before the sample mapping, the tip area function and frame compliance were calibrated using a fused silica sample of known Poisson's ratio (0.179) and elastic modulus (72.12 GPa). The resulting data set was analyzed using cumulative frequency (cf) plots to identify the mechanical properties reflecting different microstructural components following the considerations of ref. [90]. In this study, the term microstructural component refers to microstructural regions, containing different phases and can be distinguished by various microscopic investigations.

Assuming a Gaussian distribution for hardness H and Young's modulus E in each microstructural component, the sum of three cumulative Gaussian distributions with variable fraction was fitted to the cf plots. Hence, three distinct hardness values and moduli, their respective standard deviation, and a relative occurrence of each component were characterized. The mechanical properties of each individual indent were attributed to one of the microstructural components and the mapping is reconstructed accordingly. The same method of investigation was also applied to the dense ($\text{Hf}_{0.2}\text{Ta}_{0.8}$)C/SiC ceramic. The results are very similar, corroborating the analysis in this investigation.

Acknowledgements

The authors thank Prof. M. Bram and his team from the Institute for Energy and Climate Research, at the Forschungszentrum Jülich for FAST experiments and Dr. G. Schmidt from the materials and corrosion group at DECHEMA Forschungsinstitut for EPMA measurements.

Open Access funding enabled and organized by Projekt DEAL.

Conflict of Interest

The authors declare no conflict of interest.

Author Contributions

N.T.: methodology, microscopic investigation, writing—original draft preparation, visualization; G.W.: investigation (data interpretation and visualization of mechanical properties) writing—review and editing; J.B.: investigation (PDC synthesis of material), review and editing; J.W.: investigation (nanoindentation measurements and data interpretation), review and editing; N.-C.P.: conceptualization, writing—review and editing; K.B.: investigation (XRD analysis) and data interpretation (XRD pattern), writing—review and editing; R.S.: supervision, review and editing, funding acquisition; R.R.: supervision, review and editing, funding acquisition; U.K.: review and editing, supervision; M.L.: conceptualization, review and editing, supervision, funding acquisition; A.P.: conceptualization, review and editing, supervision, funding acquisition.

Data Availability Statement

The data that support the findings of this study are available on request from the corresponding author. The data are not publicly available due to privacy or ethical restrictions.

Keywords

field-assisted sintering technique, microstructures, nanoindentation, polymer-derived ceramics, silicon carbide, transition metal carbides, ultra-high temperature ceramics

Received: November 6, 2023

Revised: February 2, 2024

Published online: February 29, 2024

- [1] W. G. Fahrenholtz, G. E. Hilmas, *Scr. Mater.* **2017**, 129, 94.
- [2] A. Paul, D. D. Jayaseelan, S. Venugopal, E. Zapata-Solvas, J. Binner, B. Vaidyanathan, A. Heaton, P. Brown, W. E. Lee, *Am. Ceram. Soc. Bull.* **2012**, 2021, 91.
- [3] S. A. Ghaffari, M. A. Faghihi-Sani, F. Golestani-Fard, H. Mandal, *J. Eur. Ceram. Soc.* **2013**, 33, 1479.
- [4] E. Wuchina, E. Opila, M. Opeka, B. Fahrenholtz, I. Talmy, *Electrochem. Soc. Interface* **2007**, 16, 30.
- [5] Q. Wen, Z. Yu, Y. Xu, Y. Lu, C. Fasel, K. Morita, O. Guillon, G. Buntkowsky, E. Ionescu, R. Riedel, *J. Mater. Chem. C* **2018**, 6, 855.
- [6] B. Papendorf, K. Nonnenmacher, E. Ionescu, H.-J. Kleebe, R. Riedel, *Small* **2011**, 7, 970.
- [7] R. Orrù, G. Cao, *Materials* **2013**, 6, 1566.
- [8] Q. Wen, Z. Yu, R. Riedel, E. Ionescu, *J. Eur. Ceram. Soc.* **2020**, 40, 3499.
- [9] A. Bellosi, F. Monteverde, D. Sciti, *Int. J. Appl. Ceram.* **2006**, 3, 32.
- [10] H. Liu, L. Liu, F. Ye, Z. Zhang, Y. Zhou, *J. Eur. Ceram. Soc.* **2012**, 32, 3617.
- [11] *Handbook of Ceramic Hard Materials* (Ed: R. Riedel), John Wiley & Sons, Ltd., Weinheim, Germany **2008**.
- [12] M. M. Opeka, I. G. Talmy, E. J. Wuchina, J. A. Zaykoski, S. J. Causey, *J. Eur. Ceram. Soc.* **1999**, 19, 2405.
- [13] H. O. Pierson, *Handbook of Refractory Carbides and Nitrides: Properties, Characteristics, Processing, and Applications*, Noyes Publ, Westwood, NJ **1996**.
- [14] E. Wuchina, M. Opeka, S. Causey, K. Buesking, J. Spain, A. Cull, J. Routbort, F. Gutierrez-Mora, *J. Mater. Sci.* **2004**, 39, 5939.
- [15] S. Urbonaitė, M. Johnsson, G. Svensson, *J. Mater. Sci.* **2004**, 39, 1907.
- [16] M. Esfahanian, R. Oberacker, T. Fett, M. J. Hoffmann, *J. Am. Ceram. Soc.* **2008**, 91, 3803.
- [17] M. Suarez, A. Fernandez, J. L. Menendez, R. Torrecillas, H. U. J. Hennicke, R. Kirchner, T. Kessel, *Sintering Applications* (Ed: B. Ertug), InTech; Nişantaşı University, Turkey **2013**.
- [18] C. Zhang, A. Gupta, S. Seal, B. Boesl, A. Agarwal, *J. Am. Ceram. Soc.* **2017**, 100, 1853.
- [19] S. D. Oguntuyi, O. T. Johnson, M. B. Shongwe, *Met. Mater. Int.* **2021**, 27, 2146.
- [20] W. C. Tripp, H. H. Davis, H. C. Graham, *Am. Ceram. Soc. Bull.* **1973**, 52, 612.
- [21] F. Monteverde, A. Bellosi, *Adv. Eng. Mater.* **2004**, 6, 331.
- [22] F. Monteverde, A. Bellosi, *Scr. Mater.* **2002**, 46, 223.
- [23] D. Sciti, L. Silvestroni, S. Guicciardi, D. D. Fabbri, A. Bellosi, *J. Mater. Res.* **2009**, 24, 2056.
- [24] L. Silvestroni, D. Sciti, J. Kling, S. Lauterbach, H.-J. Kleebe, *J. Am. Ceram. Soc.* **2009**, 92, 1574.
- [25] D. Sciti, M. Brach, A. Bellosi, *J. Mater. Res.* **2005**, 20, 922.
- [26] K. A. Kane, B. A. Pint, D. Mitchell, J. A. Haynes, *J. Eur. Ceram. Soc.* **2021**, 41, 6130.
- [27] N. S. Jacobson, *J. Am. Ceram. Soc.* **1993**, 76, 3.
- [28] M. M. Opeka, I. G. Talmy, J. A. Zaykoski, *J. Mater. Sci.* **2004**, 39, 5887.
- [29] Z. Ren, S. B. Mujib, G. Singh, *Materials* **2021**, 14, 614.
- [30] Z. C. Eckel, C. Zhou, J. H. Martin, A. J. Jacobsen, W. B. Carter, T. A. Schaedler, *Science* **2016**, 351, 58.
- [31] B. Feng, J. Peter, C. Fasel, Q. Wen, Y. Zhang, H.-J. Kleebe, E. Ionescu, *J. Am. Ceram. Soc.* **2020**, 103, 7001.
- [32] J. Bill, F. Aldinger, *Adv. Mater.* **1995**, 7, 775.
- [33] E. Ionescu, S. Bernard, R. Lucas, P. Kroll, S. Ushakov, A. Navrotsky, R. Riedel, *Adv. Eng. Mater.* **2019**, 21, 1900269.
- [34] P. Colombo, G. Mera, R. Riedel, G. D. Sorarù, *J. Am. Ceram. Soc.* **2010**, 93, 1805.
- [35] C. Zhou, X. Gao, Y. Xu, G. Buntkowsky, Y. Ikuhara, R. Riedel, E. Ionescu, *J. Eur. Ceram. Soc.* **2015**, 35, 2007.
- [36] Q. Wen, Y. Xu, B. Xu, C. Fasel, O. Guillon, G. Buntkowsky, Z. Yu, R. Riedel, E. Ionescu, *Nanoscale* **2014**, 6, 13678.
- [37] J. Yuan, S. Hapis, H. Breitzke, Y. Xu, C. Fasel, H.-J. Kleebe, G. Buntkowsky, R. Riedel, E. Ionescu, *Inorg. Chem.* **2014**, 53, 10443.
- [38] J. Yuan, D. Li, K. E. Johanns, C. Fasel, K. Durst, H.-J. Kleebe, Z. Shen, R. Riedel, E. Ionescu, *J. Eur. Ceram. Soc.* **2017**, 37, 5157.
- [39] R. Sujith, A. B. Kousaalya, R. Kumar, *J. Am. Ceram. Soc.* **2011**, 94, 2788.
- [40] R. Sujith, R. Kumar, *Ceram. Int.* **2013**, 39, 9743.
- [41] Y. Lyu, H. Tang, G. Zhao, *J. Eur. Ceram. Soc.* **2020**, 40, 324.
- [42] E. Ionescu, C. Linck, C. Fasel, M. Müller, H.-J. Kleebe, R. Riedel, *J. Am. Ceram. Soc.* **2010**, 93, 241.
- [43] D. Pizon, L. Charpentier, R. Lucas, S. Foucaud, A. Maître, M. Balat-Pichelin, *Ceram. Int.* **2014**, 40, 5025.
- [44] H. Laadoua, N. Pradeilles, R. Lucas, S. Foucaud, W. J. Clegg, *J. Eur. Ceram. Soc.* **2020**, 40, 1811.
- [45] A. Lale, V. Proust, M. C. Bechelany, A. Viard, S. Malo, S. Bernard, *J. Eur. Ceram. Soc.* **2017**, 37, 5167.
- [46] N. Thor, J. Bernauer, N.-C. Petry, E. Ionescu, R. Riedel, A. Pundt, H.-J. Kleebe, *J. Eur. Ceram. Soc.* **2022**, 43, 1417.
- [47] F. Guillard, A. Allemand, J.-D. Lulewicz, J. Galy, *J. Eur. Ceram. Soc.* **2007**, 27, 2725.
- [48] P. Cavaliere, *Spark Plasma Sintering of Materials: Advances in Processing and Applications*, Springer International Publishing AG, Cham **2019**.
- [49] R. Marder, C. Estournès, G. Chevallier, R. Chaim, *Scr. Mater.* **2014**, 82, 57.
- [50] Z. A. Munir, U. Anselmi-Tamburini, M. Ohyanagi, *J. Mater. Sci.* **2006**, 41, 763.
- [51] O. Guillon, J. Gonzalez-Julian, B. Dargatz, T. Kessel, G. Schierning, J. Räthel, M. Herrmann, *Adv. Eng. Mater.* **2014**, 16, 830.
- [52] C. Manière, G. Lee, E. A. Olevsky, *Sci. Rep.* **2017**, 7, 15071.
- [53] Q. Wen, R. Riedel, E. Ionescu, *Corros. Sci.* **2018**, 145, 191.
- [54] Q. Wen, R. Riedel, E. Ionescu, *Adv. Eng. Mater.* **2019**, 21, 1800879.
- [55] A. Nisar, C. Zhang, B. Boesl, A. Agarwal, *Ceram. Int.* **2023**, 49, 783.
- [56] M. Li, Q. Xu, L. Wang, *Key Eng. Mater.* **2012**, 512–515, 635.
- [57] H. Li, Y. Yu, B. Fang, P. Xiao, S. Wang, *J. Eur. Ceram. Soc.* **2022**, 42, 4651.
- [58] S. J. McCormack, K.-P. Tseng, R. J. K. Weber, D. Kapush, S. V. Ushakov, A. Navrotsky, W. M. Kriven, *J. Am. Ceram. Soc.* **2019**, 102, 4848.
- [59] A. Nisar, C. Zhang, B. Boesl, A. Agarwal, *Ceramics* **2021**, 4, 20.
- [60] B. Román-Manso, M. Belmonte, M. I. Osendi, P. Miranzo, *J. Am. Ceram. Soc.* **2015**, 98, 2745.
- [61] S. K. Sharma, M. Fides, P. Hvizdoš, M. J. Reece, S. Grasso, *Silicon* **2022**, 14, 7377.
- [62] Bureau international des poids et mesures, *Guide to the Expression of Uncertainty in Measurement*, International Organization for Standardization, Genève **1993**.
- [63] Q. Wen, Z. Yu, R. Riedel, *Prog. Mater. Sci.* **2020**, 109, 100623.
- [64] O. Guillon, W. Rheinheimer, M. Bram, *Adv. Eng. Mater.* **2023**, 25, 2201870.

- [65] S. Grasso, E.-Y. Kim, T. Saunders, M. Yu, A. Tudball, S.-H. Choi, M. Reece, *Cryst. Growth Des.* **2016**, *16*, 2317.
- [66] H.-J. Kleebe, K. Nonnenmacher, E. Ionescu, R. Riedel, *J. Am. Ceram. Soc.* **2012**, *95*, 2290.
- [67] K. Nonnenmacher, H.-J. Kleebe, J. Rohrer, E. Ionescu, R. Riedel, *J. Am. Ceram. Soc.* **2013**, *96*, 2058.
- [68] P. Raj, G. S. Gupta, V. Rudolph, *Thermochim. Acta* **2020**, *687*, 178577.
- [69] J. Gu, S.-H. Lee, H.-S. Lee, J.-S. Kim, *J. Eur. Ceram. Soc.* **2021**, *41*, 2297.
- [70] A. Saha, R. Raj, *J. Am. Ceram. Soc.* **2007**, *90*, 578.
- [71] H.-J. Kleebe, C. Turquat, G. D. Sorarù, *J. Am. Ceram. Soc.* **2001**, *84*, 1073.
- [72] A. Maître, A. V. Put, J. P. Laval, S. Valette, G. Trolliard, *J. Eur. Ceram. Soc.* **2008**, *28*, 1881.
- [73] L. Stobierski, A. Gubernat, *Ceram. Int.* **2003**, *29*, 355.
- [74] L. Stobierski, A. Gubernat, *Ceram. Int.* **2003**, *29*, 287.
- [75] A. V. Rau, K. Knott, K. Lu, *Mater. Chem. Front.* **2021**, *5*, 6530.
- [76] D. Pandey, P. Krishna, *Prog. Cryst. Growth Charact.* **1983**, *7*, 213.
- [77] U. Kaiser, A. Chuvilin, W. Richter, *Ultramicroscopy* **1999**, *76*, 21.
- [78] R. Dong, W. Yang, P. Wu, M. Hussain, Z. Xiu, G. Wu, P. Wang, *Mater. Charact.* **2015**, *103*, 37.
- [79] Y. Ryu, Y. Tak, K. Yong, *Nanotechnology* **2005**, *16*, S370.
- [80] F. Li, G. Wen, *J. Mater. Sci.* **2007**, *42*, 4125.
- [81] A. Putnis, *Introduction to Mineral Sciences*, Cambridge University Press, Cambridge **2005**.
- [82] A. Nino, T. Hirabara, S. Sugiyama, H. Taimatsu, *IJRMHM* **2015**, *52*, 203.
- [83] L. G. Radosevich, W. S. Williams, *J. Am. Ceram. Soc.* **1970**, *53*, 30.
- [84] O. Cedillos-Barraza, S. Grasso, N. A. Nasiri, D. D. Jayaseelan, M. J. Reece, W. E. Lee, *J. Eur. Ceram. Soc.* **2016**, *36*, 1539.
- [85] L. Silvestroni, A. Bellosi, C. Melandri, D. Sciti, J. X. Liu, G. J. Zhang, *J. Eur. Ceram. Soc.* **2011**, *31*, 619.
- [86] T. B. Holland, J. F. Löffler, Z. A. Munir, *J. Appl. Phys.* **2004**, *95*, 2896.
- [87] R. Marder, R. Chaim, C. Estournès, *Mater. Sci. Eng., A* **2010**, *527*, 1577.
- [88] S. G. Huang, K. Vanmeensel, O. Malek, O. van der Biest, J. Vleugels, *Mater. Sci. Eng., A* **2011**, *528*, 1302.
- [89] V. Medri, F. Monteverde, A. Balbo, A. Bellosi, *Adv. Eng. Mater.* **2005**, *7*, 159.
- [90] N. X. Randall, M. Vandamme, F.-J. Ulm, *J. Mater. Res.* **2009**, *24*, 679.
- [91] Q. Wen, Z. Yu, R. Riedel, E. Ionescu, *J. Eur. Ceram. Soc.* **2021**, *41*, 3002.
- [92] D. Sciti, S. Guicciardi, M. Nygren, *J. Am. Ceram. Soc.* **2008**, *91*, 1433.
- [93] B. Ye, Y. Chu, K. Huang, Da Liu, *J. Am. Ceram. Soc.* **2019**, *102*, 919.
- [94] M. Ma, Y. Sun, Y. Wu, Z. Zhao, L. Ye, Y. Chu, *J. Am. Ceram. Soc.* **2022**, *105*, 606.
- [95] Q. Wen, Z. Yu, X. Liu, S. Bruns, X. Yin, M. Eriksson, Z. J. Shen, R. Riedel, *J. Mater. Chem. C* **2019**, *7*, 10683.
- [96] S. Hayun, V. Paris, R. Mitrani, S. Kalabukhov, M. P. Dariel, E. Zaretsky, N. Frage, *Ceram. Int.* **2012**, *38*, 6335.
- [97] A. Datye, L. Li, W. Zhang, Y. Wei, Y. Gao, G. M. Pharr, *J. Appl. Mech.* **2016**, *83*, 091003-1.
- [98] S. Gates-Rector, T. Blanton, *Powder Diffr.* **2019**, *34*, 352.
- [99] C. A. Schneider, W. S. Rasband, K. W. Eliceiri, *Nat. Methods* **2012**, *9*, 671.
- [100] M. Lau, F. Morgenstern, R. Hübscher, A. Knospe, M. Herrmann, M. Döring, W. Lippmann, *Pract. Metallogr.* **2020**, *57*, 752.
- [101] K. L. Scrivener, *MRS Proc.* **1988**, *137*, 129.
- [102] H. Salmang, H. Scholze, *Keramik. 7., vollständig neubearbeitete und erweiterte Auflage, hrsg. Von Reiner Telle*, Springer, Berlin **2007**.
- [103] P. Sudharshan Phani, W. C. Oliver, *Mater. Des.* **2019**, *164*, 107563.
- [104] S. Guicciardi, A. Balbo, D. Sciti, C. Melandri, G. Pezzotti, *J. Eur. Ceram. Soc.* **2007**, *27*, 1399.